On the construction of a direct numerical simulation of a breaking inertia-gravity wave in the upper-mesosphere

Mark D. Fruman[1], Sebastian Remmler[2], Ulrich Achatz[1], Stefan Hickel[2]

Corresponding author: U. Achatz, Institute for Atmosphere and Environment, Goethe-University Frankfurt, Altenhöferallee 1, 60438 Frankfurt am Main, Germany. (achatz@iau.uni-frankfurt.de)

[1]Institute for Atmosphere and Environment, Goethe-University Frankfurt, Frankfurt am Main, Germany.

[2]Institute of Aerodynamics and Fluid Mechanics, Technische Universität München, Munich, Germany.

Abstract. A systematic approach to the direct numerical simulation (DNS) of breaking upper-mesospheric inertia-gravity waves of amplitude close to or above the threshold for static instability is presented. Normal mode or singular vector analysis applied in a frame of reference moving with the phase velocity of the wave (in which the wave is a steady solution) is used to determine the most likely scale and structure of the primary instability and to initialize nonlinear "2.5-D" simulations (with three-dimensional velocity and vorticity fields but depending only on two spatial coordinates). Singular vector analysis is then applied to the time-dependent 2.5-D solution to predict the transition of the breaking event to three-dimensional turbulence and to initialize three-dimensional DNS. The careful choice of the computational domain and the relatively low Reynolds numbers, on the order of 25000, relevant to breaking waves in the upper mesosphere, make the three-dimensional DNS tractable with present day computing clusters. Three test cases are presented: a statically unstable low-frequency inertia-gravity wave, a statically and dynamically stable inertia-gravity wave, and a statically unstable high-frequency gravity wave. The three-dimensional DNS are compared to ensembles of 2.5-D simulations. In general the decay of the wave and generation of turbulence is faster in three dimensions, but the results are otherwise qualitatively and quantitatively similar, suggesting that results of 2.5-D simulations are meaningful if the domain and initial condition are chosen properly.

1. Introduction

Inertia-gravity waves are a ubiquitous feature of the dynamics in the atmosphere and play a pivotal role in the global circulation. They are forced mostly by flow over orography [e.g. *Smith*, 1979; *Lilly et al.*, 1982; *McFarlane*, 1987], by convection [e.g. *Chun et al.*, 2001; *Grimsdell et al.*, 2010], and by spontaneous imbalance of the mean flow in the troposphere [*O'Sullivan and Dunkerton*, 1995; *Plougonven and Snyder*, 2007], and they transport energy and momentum from the region where they are forced to the region where they are dissipated (e.g. through breaking), often thousands of kilometres away. Since the waves are filtered and refracted by the environment through which they propagate, their effects are highly nonuniform. Various phenomena, such as the cold summer mesopause [*Hines*, 1965; *Lindzen*, 1973] and the quasi-biennial oscillation in the equatorial stratosphere [e.g. *Baldwin et al.*, 2001], cannot be explained nor reproduced in weather and climate simulations without accounting for the effect of gravity waves [see *Fritts and Alexander*, 2003, for an overview of gravity waves in the middle atmosphere]. In almost all cases, this is done through rather crude and extensively tuned *parameterizations* based on combinations of linear wave theory [beginning with *Lindzen*, 1981], empirical observations of time-mean energy spectra [e.g. *Hines*, 1997], and very simplified treatments of the breaking process. See *Kim et al.* [2003] and *McLandress* [1998] for reviews of the various standard parameterization schemes.

Inertia-gravity wave breaking involves time scales from seconds to hours and spatial scales from metres to tens of kilometres. It is therefore a demanding problem for both observational and computational investigation. The representation of small-scale turbulence in wave-breaking simulations and of wave breaking in weather and climate simulations represent two important but separate parameterization problems in atmospheric science. The former is the goal of Large Eddy Simulation (LES). To be trusted, an LES scheme must be tested against turbulence-resolving Direct Numerical Simulation (DNS). The purpose of the present study is to describe a systematic strategy for constructing such DNS and to provide DNS for a selection of waves with different characteristics. To qualify as DNS, a simulation of a turbulent flow must resolve scales smaller than the Kolmogorov length η, which depends on the kinematic viscosity ν and the maximum rate of kinetic energy dissipation. η represents the scale below which molecular viscosity and diffusion dominate over inertial effects and energy is removed from the system or converted to heat. For realistic flows in the troposphere, η is on the order of millimetres [*Vallis*, 2006] so for gravity waves with wavelengths on the order of kilometres DNS is impossible. One case where DNS is possible is waves in the upper mesosphere (about 80 km altitude), where due to the extremely low ambient density, ν is about 1 m^2s^{-1} in the U.S. Standard Atmosphere [*NOAA et al.*, 1976]. *Remmler et al.* [2013] found from simulation of a breaking statically unstable 3 km inertia-gravity wave a Kolmogorov length of between 1 m and 3 m so that a 3-D DNS could be achieved with on the order of 10^9 gridcells.

There have been a number of recent numerical studies of breaking gravity waves. *Fritts et al.* [2009a, b] performed high resolution DNS of high-frequency gravity waves (with periods of a few times the background buoyancy period) with amplitudes slightly above and slightly below the threshold for convective instability. They found that both waves break down to about a third of their initial amplitude within one or two wave periods and that the early phase of wave breaking is dominated by turbulent three-dimensional motion, while wave-wave interactions between the primary wave and secondary waves excited by the breaking persist for many wave periods. *Fritts et al.* [2013] and *Fritts and Wang* [2013] performed highly resolved, high Reynolds number DNS of a monochromatic gravity wave breaking due to interaction with a vertically varying "fine-structure" shear flow, finding that the direction of the fine-structure flow relative to the plane of the wave strongly affected the degree to which the gravity wave broke down into turbulence.

The above studies neglect the Coriolis effect and thus the velocity field of the primary gravity wave is strictly in the plane of phase propagation. The propagation of *inertia*-gravity waves, on the other hand, is maintained by both the vertical restoring force due to the stratification and the horizontal restoring force due to the Coriolis effect (the vertical component of the Coriolis force is typically neglected). Since in the atmosphere the former is much stronger than the latter, waves with steep phase propagation, with their nearly horizontal fluid parcel motions strongly influenced by the Coriolis force, have much lower frequency than waves with shallow phase propagation. Instability and breaking are very different for inertia-gravity waves of different frequencies [*Achatz*, 2005, 2007a, b; *Lelong and Dunkerton*, 1998] so it is difficult to extrapolate any conclusions from a DNS study to waves with higher or lower frequency. *Remmler et al.* [2013] produced a DNS of a statically unstable low-frequency inertia-gravity wave (referred to as case I later in this paper). The low-frequency wave decays much less than a high-frequency wave, only to about three quarters of its initial amplitude within one wave period, about 8 hours in that case. Also, the distribution of turbulent energy dissipation is much more inhomogeneous and intermittent than for a high-frequency wave.

Other recent studies have simulated not just one wavelength of a monochromatic wave in a triply periodic domain (as is done in the present work), but the more realistic case of a train of waves propagating through a variable background as they break. *Lund and Fritts* [2012] considered waves propagating through the thermosphere, their amplitude growing due to the decreasing density and changing due to the height-dependent stratification and chemical composition. *Liu et al.* [2010] considered waves excited at the surface of the ocean propagating downward through the thermocline. These studies must inevitably sacrifice model resolution to accommodate multiple wavelengths but are essential if conclusions from the more fully resolved idealized DNS are to be applied to more practical problems such as the parameterization of wave breaking in general circulation models, where a monochromatic inertia-gravity wave is unlikely to occur in isolation, especially at the amplitude for convective instability.

Since a DNS of a breaking inertia-gravity wave is computationally expensive, time-consuming, and produces a dauntingly complex and nonlinear result, it is important to choose the domain and parameters carefully. The present work describes a systematic, hierachical approach to analyzing an inertia-gravity wave breaking event, combining linear modal analysis with two- and three-dimensional nonlinear simulation. Aspects of this procedure have already been published in *Achatz* [2007a, b], *Fruman and Achatz* [2012] and *Remmler et al.* [2013]. Three test cases were chosen, representing waves with different inherent time scales and breaking behaviour.

The analysis is greatly simplified if one works with the Boussinesq approximation on an f-plane with a constant background Brunt-Väisälä frequency, enabling the use of periodic boundary conditions in any three orthogonal directions, one of which is usually chosen parallel to the direction of phase-propagation of the wave. While obviously not realistic for a general description of the dynamics in the mesosphere, one might justify the Boussinesq approximiation as long as the wavelength of the wave is small compared to the density scale height and the breaking process is fast compared to the vertical group propagation of the wave.

The method proceeds in four stages: (1) solution (in the form of normal modes or singular vectors) of the equations linearized about the basic state wave, determining the primary instability structures; (2) nonlinear two-dimensional (in space) numerical solution of the full equations using the result of stage 1 as initial condition; (3) solution in the form of singular vectors (varying in the remaining spatial direction) of the Boussinesq equations linearized about the time-dependent result of stage 2; (4) three-dimensional DNS using the linear solutions from stages 1 and 3 as initial condition and their wavelengths for the size of the computational domain. In some cases the resulting computational domain is relatively narrow in either the streamwise or the spanwise direction and therefore the three-dimensional DNS is comparatively very efficient. Implicit in the strategy is that there is a temporal and/or spatial scale separation between the primary and secondary instabilities so that the nonlinear two-dimensional solution (stage 2) resembles the realistic (three-dimensional) evolution for a short time while secondary instabilities – different in scale and character from the primary instabilities calculated in stage 1 – develop. This is the advantage of the approach over simply initializing three-dimensional DNS with mutually orthogonal primary perturbations.

The paper is organized as follows. Section 2 presents the governing equations, the monochromatic inertia-gravity wave solution and the rotated coordinate system used.

Section 3 describes in detail the four-stage approach to gravity-wave breaking analysis. Section 4 presents the three test cases. The numerical methods used are explained in section 5. The results of the analyses are presented in section 6. Appendices elaborate on the calculation of normal modes and singular vectors, on projection of the evolving solution onto the original wave, and on the computing resources used for the 3-D DNS.

2. Governing Equations and the Gravity Wave Solution

Without loss of generality we may assume that the monochromatic inertia-gravity wave is propagating in the x-z plane and let Θ be its angle of phase propagation with respect to the x-axis. The problem is best solved in a reference frame (ξ, y, ζ) rotated about the y-axis through an angle $\pi/2 - \Theta$ so that the wave-vector of the gravity wave is parallel to the ζ-axis (see left panel of figure 1). That is,

$$\xi = x \sin\Theta - z\cos\Theta, \tag{1a}$$

$$\zeta = x\cos\Theta + z\sin\Theta. \tag{1b}$$

The Boussinesq equations may be written

$$\frac{\partial \boldsymbol{v}}{\partial t} + (\boldsymbol{v}\cdot\nabla)\,\boldsymbol{v} = b\hat{\boldsymbol{e}}_z - f\hat{\boldsymbol{e}}_z \times \boldsymbol{v} - \nabla p + \nu\nabla^2\boldsymbol{v}, \tag{2a}$$

$$\frac{\partial b}{\partial t} + (\boldsymbol{v}\cdot\nabla)\, b = -N^2\hat{\boldsymbol{e}}_z\cdot\boldsymbol{v} + \mu\nabla^2 b, \tag{2b}$$

$$\nabla\cdot\boldsymbol{v} = 0, \tag{2c}$$

where $\boldsymbol{v} = (u_\xi, v, w_\zeta)$ is the fluid velocity, b is buoyancy, p is pressure normalized by a constant background density, $\hat{\boldsymbol{e}}_z$ is the unit vector in the true vertical direction, N is the Brunt-Väisälä frequency, f is the Coriolis parameter, and ν and μ are the kinematic viscosity and thermal diffusivity respectively.

An inertia-gravity wave propagating in the x-z plane at an angle Θ to the x-axis and with upward group velocity may be written in the form

$$
\begin{aligned}
[u_\xi, v, w_\zeta, b] &= [U_{\xi 0}, V_0, W_{\zeta 0}, B_0] \\
&\equiv \mathrm{Re}\left\{ a \left[\frac{iK\omega}{km}, \frac{f}{k}, 0, -\frac{N^2}{m} \right] e^{i\phi} \right\},
\end{aligned}
\tag{3}
$$

where K is the magnitude of the wavevector, $k = K\cos\Theta$ and $m = K\sin\Theta$ are its horizontal and vertical components in the Earth frame,

$$
\omega = -\sqrt{f^2 \sin^2\Theta + N^2 \cos^2\Theta}
\tag{4}
$$

is the frequency, and $\phi = K\zeta - \omega t$ is the wave phase. The nondimensional (complex) wave amplitude a is defined such that a wave with $|a| = 1$ is neutral with respect to static instability at its least stable point, namely where the vertical gradient of total potential temperature is least. Equation (3) is an exact solution to (2) in the inviscid ($\nu = \mu = 0$) limit. When the Prandtl number is unity (i.e. $\nu = \mu$), the solution decays exponentially with time such that

$$
a(t) = a(0) e^{-\nu K^2 t}.
\tag{5}
$$

In the midlatitude mesosphere, N is about one hundred times larger than f, so the properties of the wave are very sensitive to Θ. A wave with Θ close to 90° has a relatively low frequency – close to f – and elliptically polarized velocity in the streamwise-spanwise (ξ-y) plane, i.e. u_ξ and v are of similar amplitude. Since f strongly affects the form of these waves, we call them inertia-gravity waves (IGW). A wave with shallower phase propagation has much higher frequency, approximately equal to $N\cos\Theta$, and a linearly polarized transverse velocity field ($|v| \ll |u|$). We call such waves high-frequency gravity waves (HGW) (strictly speaking, these are also inertia-gravity waves but rotation plays a negligible role). *Lelong and Dunkerton* [1998] and *Achatz* [2005] showed that the nature of the instabilities of the two categories of waves are markedly different. This is primarily because of the influence of the transverse velocity component – large in the IGW and small in the HGW – which has maximum vertical shear at the levels of maximum buoyancy gradient, and because of the important role played by horizontal buoyancy gradients and horizontal velocity shear in the HGW.

3. Four-stage Approach to the Simulation of Gravity-Wave Breaking

In order to quantify the temporal and spatial scales of gravity-wave breaking and to design a meaningful but still computationally tractable (and economical) 3-D DNS, we employ the following four-stage combination of linear and nonlinear analysis.

3.1. Primary instability analysis and 2.5-dimensional DNS

The first step is to perform a large number of one-dimensional linear calculations to determine the wavelength, orientation and spatial structure of the most unstable perturbations to the gravity wave.

The Boussinesq equations (2) are linearized about the gravity wave (3) to yield the system

$$\frac{D'u'_\xi}{Dt} + w'_\zeta \frac{\mathrm{d}U_{\xi 0}}{\mathrm{d}\phi} + \cos\Theta b' - f\sin\Theta v' + \frac{\partial p'}{\partial \xi} = \nu\nabla^2 u'_\xi, \tag{6a}$$

$$\frac{D'v'}{Dt} + w'_\zeta \frac{\mathrm{d}V_0}{\mathrm{d}\phi} + f\left(\sin\Theta u'_\xi + \cos\Theta w'_\zeta\right) + \frac{\partial p'}{\partial y} = \nu\nabla^2 v', \tag{6b}$$

$$\frac{D'w'_\zeta}{Dt} - \sin\Theta b' - f\cos\Theta v' + K\frac{\partial p'}{\partial \phi} = \nu\nabla^2 w'_\zeta, \tag{6c}$$

$$\frac{D'b'}{Dt} + w'_\zeta \frac{\mathrm{d}B_0}{\mathrm{d}\phi} + N^2\left(-\cos\Theta u'_\xi + \sin\Theta w'_\zeta\right) = \mu\nabla^2 b', \tag{6d}$$

$$\frac{\partial u'_\xi}{\partial \xi} + \frac{\partial v'}{\partial y} + K\frac{\partial w'_\zeta}{\partial \phi} = 0, \tag{6e}$$

where $[u'_\xi, v', w'_\zeta, b']$ is a small departure from (3) and

$$\frac{D'}{Dt} \equiv \frac{\partial}{\partial t} + U_{\xi 0}\frac{\partial}{\partial \xi} + V_0\frac{\partial}{\partial y} - \omega\frac{\partial}{\partial \phi}. \tag{7}$$

Since the coefficients of u'_ξ, v', w'_ζ and b' in (6) are independent of streamwise and spanwise position (ξ, y), solutions may be sought in the form

$$[u'_\xi, v', w'_\zeta, b'] = \Re\left\{[\hat{u}'_\xi(\phi,t), \hat{v}'(\phi,t), \hat{w}'_\zeta(\phi,t), \hat{b}'(\phi,t)]\exp\left[i(k_\xi \xi + k_y y)\right]\right\}, \tag{8}$$

where k_ξ and k_y are constants. The ansatz (8) is inserted in (6) and the resulting system of equations for $[\hat{u}'_\xi, \hat{v}', \hat{w}'_\zeta, \hat{b}']$ are solved numerically (see section 5).

Note that the dissipation of the gravity wave solution is neglected in (6) so that the system of equations for $[\hat{u}'_\xi, \hat{v}', \hat{w}'_\zeta, \hat{b}']$ is homogeneous and autonomous and therefore admits normal mode analysis. The approximation is valid for our test cases since the time scale of the decay of the wave, $(\nu K^2)^{-1} \approx 2$ days, is long compared to the time for which the linear model is run (5 or 7.5 minutes) and the inverse growth rates of the fastest growing modes (about 100 s).

Normal modes are solutions of (6) in which the time dependence of $[u'_\xi, v', w'_\zeta, b']$ is a complex exponential function. For statically unstable waves ($|a| > 1$), there typically exist exponentially *growing* solutions, and the normal mode with largest growth factor is the dominant linear mode. For statically and dynamically stable waves, by which we mean that the Richardson number corresponding to the solution (3), *viz*

$$Ri_{IGW} = \frac{N^2(1 + a\sin\phi)}{a^2\tan^2\Theta(\omega^2\cos^2\phi + f^2\sin^2\phi)}, \tag{9}$$

is greater than 1/4 [the sufficient condition for linear stability of a steady, stratified shear flow; see *Howard*, 1961; *Miles*, 1961], there are typically no exponentially growing normal modes, so the leading singular vector for a given optimization time is calculated instead.

The leading singular vector [*Farrell and Ioannou*, 1996a, b] for a given perturbation wavelength $\lambda_{\parallel}$ and orientation angle α is defined as the perturbation whose energy (or another norm) grows by the largest factor in the given optimization time (as governed by the linearized equations). Although singular vectors necessarily consist of superpositions of normal modes, they can have large growth factors even when all normal modes are exponentially decaying, since the latter are not orthogonal (i.e. "non-normal") with respect to the energy scalar product. Details of the computation of normal modes and singular vectors are given in appendix A [see also *Achatz*, 2005, 2007a].

The second stage is to perform nonlinear two-dimensional simulations initialized with the original gravity wave and one of the "more interesting" normal modes (or singular vectors), by which is meant those with the highest linear growth rate (or growth factor). In order to perform these simulations, a second rotation of the coordinate system, this time through an angle α about the ζ-axis (right panel of figure 1) is required, leading to the new coordinates

$$x_{\parallel} = \xi \cos\alpha + y \sin\alpha, \tag{10a}$$

$$y_{\perp} = -\xi \sin\alpha + y \cos\alpha. \tag{10b}$$

and corresponding velocity components $u_{\parallel}$ and $v_{\perp}$.

Since the dynamics – in terms of, for example, the energy exchange processes – are so different for *transverse* ($\alpha = 90°$) and *parallel* ($\alpha = 0°$) perturbations [*Andreassen et al.*, 1994; *Lelong and Dunkerton*, 1998; *Achatz*, 2007a; *Fruman and Achatz*, 2012], both the leading transverse and parallel perturbations are tried even when one has a much lower linear growth rate (or growth factor) than the other. As we will see, perturbation by the mode with smaller linear growth rate (or growth factor) can have a much more profound effect on the breaking of the original wave in nonlinear simulations. These simulations are called here "2.5-dimensional" (2.5-D) because although there are only two independent spatial coordinates, the velocity and vorticity fields are three-dimensional. Since there is no conservation of enstrophy in this system (due to the vortex-tilting mechanism being active) the turbulent energy cascade is *direct* as in three-dimensional turbulence rather than inverse as in classical two-dimensional turbulence [e.g. *Kraichnan and Montgomery*, 1980].

For each 2.5-D simulation, the projection of the solution onto the original gravity wave mode [see appendix B and *Achatz*, 2007b, for details] is plotted versus time and compared to the laminar decay of an unperturbed wave (see Eq. 5). A breaking wave decays faster, at first due to energy exchange with the growing linear mode and later due to interaction with the turbulence excited by the breaking. The latter process can last much longer than the time scale of the linear perturbation and as long as the period of the original wave. The decay of the gravity wave amplitude is the quantity most relevant to parameterizations of gravity-wave drag in atmospheric models.

Other diagnostics used are the sum of the kinetic energy dissipation rate ϵ_k and the potential energy dissipation rate ϵ_p, where

$$\epsilon_k = \frac{\nu}{2}\left(\frac{\partial v_i}{\partial x_j} + \frac{\partial v_j}{\partial x_i}\right)\left(\frac{\partial v_i}{\partial x_j} + \frac{\partial v_j}{\partial x_i}\right), \tag{11a}$$

$$\epsilon_p = \frac{\mu}{N^2}\frac{\partial b}{\partial x_i}\frac{\partial b}{\partial x_i} \tag{11b}$$

(summation over repeated indices is implied), and the streamwise-spanwise-averaged energy–wavelength spectra. Note that in nature the dissipation of kinetic energy leads to localized frictional heating, an effect not considered in the present study.

3.2. Secondary instability analysis and three-dimensional DNS

The 2.5-D solution, which we write

$$[u_\parallel, v_\perp, w_\zeta, b] = \left[U_\parallel(x_\parallel,\phi,t), V_\perp(x_\parallel,\phi,t), W_\zeta(x_\parallel,\phi,t), B(x_\parallel,\phi,t)\right], \tag{12}$$

remains two-dimensional in space if not perturbed, but in nature the breaking of a gravity wave is inherently three-dimensional. Therefore, in the next stage, the 2.5-D simulations in which the gravity wave amplitude decreased by the largest amount are subjected to a secondary instability analysis. The full equations (2) are linearized about the time-dependent 2.5-D solution (12) to yield

$$\frac{D''u''_\parallel}{Dt} + \frac{\partial U_\parallel}{\partial x_\parallel}u''_\parallel + K\frac{\partial U_\parallel}{\partial \phi}w''_\zeta + \cos\alpha\cos\Theta b'' \\ - f\left(\sin\Theta v''_\perp + \sin\alpha\cos\Theta u''_\parallel\right) + \frac{\partial p''}{\partial x_\parallel} = \nu\nabla^2 u''_\parallel, \tag{13a}$$

$$\frac{D''v''_\perp}{Dt} + \frac{\partial V_\perp}{\partial x_\parallel}u''_\parallel + K\frac{\partial V_\perp}{\partial \phi}w''_\zeta - \sin\alpha\cos\Theta b'' \\ + f\left(\sin\Theta u''_\parallel + \cos\alpha\cos\Theta w''_\zeta\right) + \frac{\partial p''}{\partial y_\perp} = \nu\nabla^2 v''_\perp, \tag{13b}$$

$$\frac{D''w''_\zeta}{Dt} + \frac{\partial W_\zeta}{\partial x_\parallel}u''_\parallel + K\frac{\partial W_\zeta}{\partial \phi}w''_\zeta - \sin\Theta b'' \\ - f\left(\sin\alpha\cos\Theta u''_\parallel + \cos\alpha\cos\Theta v''_\perp\right) + K\frac{\partial p''}{\partial \phi} = \nu\nabla^2 w''_\zeta, \tag{13c}$$

$$\frac{D''b''}{Dt} + N^2\left(-\cos\alpha\cos\Theta u''_\parallel + \sin\alpha\cos\Theta v''_\perp \right. \\ \left. + \sin\Theta w''_\zeta\right) = \mu\nabla^2 b'', \tag{13d}$$

$$\frac{\partial u''_\parallel}{\partial x_\parallel} + \frac{\partial v''_\perp}{\partial y_\perp} + K\frac{\partial w''_\zeta}{\partial \phi} = 0, \tag{13e}$$

where

$$\frac{D''}{Dt} \equiv \frac{\partial}{\partial t} + U_\parallel\frac{\partial}{\partial x_\parallel} + V_\perp\frac{\partial}{\partial y_\perp} + \left(KW_\zeta - \omega\right)\frac{\partial}{\partial \phi}, \tag{14}$$

and $u''_{\parallel}$, $v''_{\perp}$, w''_{ζ}, and b'' are small perturbations from the 2.5-D basic state (12). Solutions are sought in the form

$$[u''_{\parallel}, v''_{\perp}, w''_{\zeta}, b''] = \Re\left\{[\hat{u}''_{\parallel}(x_{\parallel}, \phi, t), \hat{v}''_{\perp}(x_{\parallel}, \phi, t), \hat{w}''_{\zeta}(x_{\parallel}, \phi, t), \hat{b}''(x_{\parallel}, \phi, t)] \times \exp(ik_{\perp}y_{\perp})\right\}, \tag{15}$$

where $k_{\perp}$ is the wavenumber in the $y_{\perp}$ direction (perpendicular to the plane defined by the wavevectors of the gravity wave and the primary perturbation).

Since the coefficients in (13) are time dependent, normal mode solutions of the form (15) – i.e. solutions with complex-exponential time-dependence – do not exist. Instead, the leading singular vectors are computed for various wavelengths $\lambda_{\perp}$. This entails calculating eigenvectors involving tens to hundreds of 2.5-D linear integrations for each value of $\lambda_{\perp}$ [see *Fruman and Achatz*, 2012, for more details]. An alternative approach, used by *Klaassen and Peltier* [1985] for the related problem of secondary instabilities in Kelvin-Helmholtz billows, is to neglect the time dependence of the basic state and calculate secondary normal modes, but such an implicit assumption of time-scale separation is not necessary for computing singular vectors.

The optimization time used for the calculation of the secondary singular vectors must necessarily be relatively short, because if at the optimization time the 2.5-D solution has already become turbulent and filamented, the fastest growing linear modes will be dominated by very small-scale shear instabilities which would quickly saturate in a nonlinear simulation and in any case are not well resolved by the numerics.

The final step is to perform three-dimensional simulations initialized with the sum of the gravity wave, the primary perturbation associated with the most significant wave decay in the 2.5-D simulations, and the initial condition of a leading secondary perturbation. The wavelengths of the primary wave and the perturbations determine the size of the triply-periodic domain. The required grid size Δ depends on the intensity of the turbulence generated during the breaking process and the corresponding Kolmogorov length

$$\eta = \min\left(\nu^{3/4}\epsilon_k^{-1/4}\right), \tag{16}$$

where the minimum is over the computational domain, by the condition $\Delta < \pi\eta$ [discussed by *Yamazaki et al.*, 2002, for the case of isotropic turbulence]. Since the resolved dissipation rate ϵ_k in turn depends on the grid resolution, the necessary grid resolution must be found by repeated simulations with increasingly fine meshes until the maximum dissipation rate does not change and the condition $\Delta < \pi\eta$ is fulfilled. The results of the 3-D DNS are compared with those of the 2.5-D simulations in terms of the time-dependent projection of the full solution onto the basic wave, the global-mean dissipation of kinetic and potential energy in the system and the streamwise-spanwise-averaged energy spectra.

4. Test Cases

Results are presented for three test cases: two low-frequency inertia-gravity waves (IGW), one of amplitude above and the other of amplitude below the static stability threshold, and a statically unstable high-frequency gravity wave (HGW). All waves have wavelength 3 km and in all three cases, the f-plane is centred at 70N ($f = 1.4 \times 10^{-4}$ s) and the constant Brunt-Väisälä frequency of $N = 2 \times 10^{-2}$ s^{-1} is used. A value of 1 m^{2}s^{-1}, realistic for the upper mesosphere, is used for the kinematic viscosity ν and thermal diffusivity μ.

The low-frequency test cases use an IGW with propagation angle $\Theta = 89.5°$, corresponding to a period of 8 hours and phase speed 0.1 ms^{-1}. Case I is a statically unstable wave with initial amplitude $a_0 \equiv |a(t_0)| = 1.2$, and case II is a statically and dynamically stable wave with $a_0 = 0.86$. The basic wave for case III is a statically unstable HGW with angle of phase-propagation $\Theta = 70°$ and initial amplitude $a_0 = 1.2$. It has a period of 15 minutes and phase speed 3.3 ms^{-1}. Due to its short period and small horizontal spatial scale, rotational effects do not play an important role in the dynamics of the HGW.

The Reynolds number, defined following *Fritts and Wang* [2013] as $Re \equiv \lambda_z^2 N/2\pi\nu$, where λ_z is the vertical wavelength of the wave, is about 28000 for cases I and II and about 25000 for case III.

The atmosphere and wave parameters for the three test cases are summarized in tables 1 and 2.

5. Numerical Methods

The 2.5-D nonlinear simulations and the linear integrations required for determining the primary and secondary instability modes are performed with the numerical models developed by *Achatz* [2005, 2007a] and *Fruman and Achatz* [2012].

As described in section 3.1 and in *Achatz* [2005], primary perturbations in the form of normal modes are computed using the one-dimensional linear system (6), constructed by linearizing (2) about (3), and substituting the ansatz (8). The independent variables are the real and imaginary parts of $\hat{u}'_\xi$, $\hat{v}'$, $\hat{w}'_\zeta$, and $\hat{b}'$ evaluated on a discretized ϕ-axis (ϕ being the phase of the wave). Singular vectors additionally require the corresponding adjoint model, which was developed using the TAMC utility [*Giering and Kaminski*, 1998]. The time integration is performed using a fourth-order Runge–Kutta scheme for the first two time steps and a third-order Adams–Bashforth scheme for the rest [see *Durran*, 2010, §2.4].

The 2.5-D nonlinear simulations are performed at high enough resolution to resolve scales down to the Kolmogorov scale, here a few metres. The time integration of the system (2) is performed using the third-order Runge–Kutta scheme of *Williamson* [1980].

The secondary singular vectors are computed using a two-dimensional model to solve the system (13) with solutions of the form (15) inserted. The dependent variables are the real and imaginary parts of $\hat{u}''_{\parallel}$, $\hat{v}''_{\perp}$, $\hat{w}''_{\zeta}$, and $\hat{b}''$ evaluated on a discrete $x_{\parallel}$-ϕ grid. Again, the corresponding adjoint model required for finding singular vectors was developed with the help of TAMC.

The 3-D DNS are performed with the INCA model [*http://www.inca-cfd.com*; for details see *Remmler and Hickel*, 2012, 2013] which solves the Boussinesq equations by means of a finite-volume fractional-step method in a triply-periodic domain. For time advancement the explicit third-order Runge-Kutta scheme of *Shu* [1988] is used. The time-step is dynamically adapted to satisfy a Courant–Friedrichs–Lewy condition. The spatial discretization is based on non-dissipative central schemes with 4th order accuracy for the advective terms and 2nd order accuracy for the diffusive terms and the pressure Poisson-equation solver.

For all models, the spatial discretization is a staggered one-, two- or three-dimensional C grid, with each velocity component evaluated at a point displaced by one half grid interval in the corresponding direction relative to the buoyancy and pressure. Eigenvalues for the primary and secondary instability analyses are computed iteratively using a variant of the Arnoldi process with the Fortran library ARPACK [*Lehoucq et al.*, 1998].

In the one- and two-dimensional models, the discrete pressure Poisson equation (obtained by setting the time derivative of the divergence constraint (2c) to zero) is solved using the discrete Fourier Transform. For the 3-D multi-block simulations, the Poisson equation is solved by a Krylov subspace solver with algebraic-multigrid preconditioning.

See appendix C for the computing resources required for the 3-D DNS and the technical specifications of the machines used to perform them.

6. Results

6.1. Case I: Statically unstable IGW

The first test case is a statically unstable inertia-gravity wave with initial amplitude $a_0 = 1.2$, propagation angle 89.5° and wavelength 3 km. The wave period is 8 hours and the phase speed is 0.1 ms^{-1}.

Figure 2a shows the five-minute growth factors for the leading normal modes as a function of perturbation wavelength $\lambda_\| \equiv 2\pi(k_\xi^2 + k_y^2)^{-1/2}$ and orientation angle $\alpha \equiv \tan^{-1}(k_y/k_\xi)$. The peaks in the growth factor occur for the limiting cases of parallel ($\alpha = 0$) and transverse ($\alpha = 90°$) perturbations. Their spatial structure can be gleaned from figure 2d, showing the perturbation energy density as a function of ϕ. The perturbations are normalized such that the ratio A_1 of the maximum perturbation energy density in the domain to the (uniform) energy density in the basic state is 0.05. The faster growing of the two modes (indeed the fastest mode overall) is the leading parallel normal mode. It has very short wavelength (316 m) and its energy is very localized near the level of maximum static instability $\phi = 3\pi/2$. The leading transverse normal mode has wavelength longer than that of the original wave ($\lambda_\| = 3.981$ km) and its energy is distributed throughout the domain.

Figure 2g shows the projection of the 2.5-D nonlinear solution on the original gravity wave as a function of time for simulations initialized with the wave plus either the leading parallel or the leading transverse normal mode, as well as the range of results from ensembles of simulations with additional small amplitude random noise (white noise smoothed with a running-mean with window of width 50 m in the $x_\parallel$ and ζ directions). For comparison, the curve showing the viscous amplitude decay of the unperturbed wave (see Eq. 5) is plotted with a dash-dot line. Despite the smaller linear growth rate of the initial perturbation, the wave perturbed by the transverse normal mode decays more than the wave perturbed by the parallel normal mode. The wave breaking lasts on the order of one half of a wave period and involves intermittent sharp drops in amplitude (these correspond to "bursts" of enhanced total energy dissipation, discussed below, see figure 6). The intermittency seems to be associated with the phase-propagation of the wave (especially the layer of weakest static stability) through the inhomogeneous field of turbulence excited by the initial instability. Because it showed the most significant wave breaking, we focus on the simulation initialized with the transverse normal mode for the secondary instability analysis and 3-D DNS.

Figure 3 shows the growth factors of the leading five-minute secondary singular vectors versus perturbation wavelength $\lambda_\perp$. Also shown are the five-minute growth factors for an ensemble of linear integrations initialized with a random perturbation with a $k^{-5/3}$ energy spectrum. The ensemble mean has a peak near $\lambda_\perp = 400$ m. The leading secondary singular vector has a somewhat longer wavelength, but for $\lambda_\perp > 400$ m, the growth factor does not change much with wavelength. The $\lambda_\perp = 400$ m singular vector was therefore used to initialize the 3-D DNS. Figure 4 shows the structure of the real part of the $\hat{w}''_\zeta$

field of the 400 m secondary singular vector at the initial and optimization time ($\tau = 5$ minutes) plotted over the time-dependent basic state velocity and buoyancy fields. Note that the energy associated with the secondary singular vector – like the parallel primary normal mode – is initially concentrated near the level of maximum negative basic-state buoyancy gradient. Unlike the primary normal mode, the structure of the singular vector evolves with time to extract most efficiently both potential energy (through interaction with the buoyancy gradient) and kinetic energy (through interaction with the wind shear) from the basic state. At the optimization time, the region of maximum energy density in the secondary singular vector straddles the line of maximum $V_\perp$ in the basic state. It is growing through the Orr mechanism associated with shear in the background velocity component parallel to the direction in which the perturbation varies (in this case $y_\perp$). See *Fruman and Achatz* [2012] for details, in particular their figures 8 and 9.

3-D DNS initialized with the IGW ($\lambda = 3$ km), the leading transverse primary normal mode ($\lambda_\parallel = 3.981$ km), and the leading secondary singular vector with $\lambda_\perp = 400$ m were run with a grid spacing Δ of about 3 m (full resolution) and 6 m (coarse) in all three directions. The amplitude for the secondary singular vector A_2, defined here as the maximum perturbation energy density divided by the maximum basic-state energy density, was 0.02. It was shown by *Remmler et al.* [2013] that only in the fully resolved simulation was the Kolmogorov length never smaller than Δ/π but that the results of the two simulations were otherwise extremely similar (hence grid-converged). Figure 5 shows the initial buoyancy field from the full resolution simulation and a snapshot at $t = 695$ s of the buoyancy field together with the kinetic energy dissipation ϵ_k. At the instant shown, very early in the simulation, turbulence has already developed in the upper half of the wave (i.e. the less stable half) and not in the lower half, but the energy density is not strongly correlated with the buoyancy gradient (velocity shear has a strong influence). Note that the figure is plotted in the reference frame moving with the wave. The decay of the wave amplitude with time and the global mean of the total energy dissipation $\epsilon_k + \epsilon_p$ from the ensemble of 2.5-D simulations and from the 3-D DNS are shown in figure 6. The initial burst of turbulence is more intense in the 3-D DNS, and the wave decays more rapidly. On the other hand, in the 2.5-D simulations the initial turbulence is more sustained – the energy decay rate is greater for $t \gtrsim 30$ minutes, and the total reduction in wave amplitude over the length of the whole simulation is greater. Figure 7 shows the streamwise and spanwise averaged total energy dissipation as a function of ζ and time from the fully resolved 3-D DNS and the 2.5-D simulations without additional noise. Again, the plot is in the reference frame moving with the phase velocity of the wave. In the first 40 minutes of the 3-D simulation the turbulent dissipation is distributed throughout the domain after which it dies out in the statically stable half. In the 2.5-D simulation dissipation is sustained also in the stable half. In analysing 2.5-D simulations of a similar unstable IGW, *Achatz* [2005, 2007a] attributed the dissipation in the stable region to small-scale waves propagating away from the unstable region and encountering a critical level. After about one half of a wave period (about 4 hours), there is an episode of enhanced energy dissipation in the 3-D DNS and a corresponding dip in the wave amplitude (cf. figure 6). At this time the point of minimum static stability in the original wave has propagated down to the level initially occupied by the most stable point. The dashed black line in figure 7 represents a point fixed in space. Evidently residual turbulence in the stable part of the wave left over from the early phase of the breaking is stirred up when it interacts with the unstable part of the wave. This is discussed in more depth in *Remmler et al.* [2013]. The dark-grey contours in figure 7 show the isoline $Ri = 1/4$, where

$$Ri = \frac{N^2 + \overline{\partial b/\partial z}}{\overline{(\partial u/\partial z)}^2 + \overline{(\partial v/\partial z)}^2} \tag{17}$$

is the Richardson number (the overbars indicate the streamwise-spanwise mean,

$$u = u_\parallel \cos\alpha \sin\Theta - v_\perp \sin\alpha \sin\Theta + w_\zeta \cos\Theta \tag{18a}$$

$$v = u_\parallel \sin\alpha + v_\perp \cos\alpha \tag{18b}$$

are the horizontal velocity components in the Earth frame, and

$$\frac{\partial}{\partial z} = -\cos\alpha\cos\Theta\frac{\partial}{\partial x_\parallel} + \sin\alpha\cos\Theta\frac{\partial}{\partial y_\perp} + \sin\Theta\frac{\partial}{\partial \zeta} \tag{19}$$

is the vertical derivative in the Earth frame). Most of the dissipation occurs in regions of $Ri < 1/4$. This does not necessarily indicate a causal relationship (along the lines of a Kelvin-Helmholtz type instability) since turbulence necessarily entails large local velocity shear, which implies small values of Ri.

Figure 8 shows the streamwise and spanwise averaged energy spectra at times of peak energy dissipation in the 2.5-D (ensemble) and coarse resolution 3-D simulations and near the end of the simulations. Also shown are the spectra from the initial conditions, which are identical in 2.5-D and 3-D except for the effect of the secondary singular vector perturbation. At the moment of maximum energy dissipation in 3-D (0.39 hours), the 2.5-D and 3-D spectra are very similar, both showing energy having moved to small scales and a $k^{-5/3}$ inertial range forming, characteristic of 3-D isotropic turbulence. The 3-D spectrum shows more energy at the smallest scales, which is what one would expect given it has more possibilities for vortex tilting and stretching and therefore a more efficient downscale energy cascade.

The spectra at the time of the second burst of dissipation in 2.5-D (1.39 hours) are quite different in 2.5-D and 3-D. There is much more energy in the smaller scales in the 2.5-D simulation, the 3-D simulation having "burned itself out" more quickly. The energy in the largest scale (which contains the original wave) is, however, almost the same in the two simulations. Both of these observations are consistent with figure 6: the dissipation at 1.39 hours is much less in 3-D (right panel), but the graphs of the projection onto the IGW intersect at about that time (left panel).

The 2.5-D spectra at 1.39 hours exhibit a clear k^{-3} inertial range behaviour. This spectral slope has been found in observations of the atmosphere [*Cot*, 2001] and in numerical studies [e.g. *Carnevale et al.*, 2001; *Brethouwer et al.*, 2007; *Remmler and Hickel*, 2013] to be characteristic of the "buoyancy range" in stratified turbulence. The 3-D spectral slope at the same time is something in between k^{-3} and $k^{-5/3}$, representing neither completely isotropic nor fully stratified turbulence. In the 2.5-D ensemble the spectra remain close to k^{-3} in the range between 100 m and 1000 m until about $t \approx 4.5$ hours (not shown), which is about as long as the turbulent dissipation persists in the stable half of the domain (compare with figure 7). This causes the turbulence to be, on average, much more strongly affected by stratification than in the 3-D DNS, where significant turbulence persists only in the unstable half of the domain. Consequently, the spectral slope in the 3-D DNS changes multiple times between $k^{-5/3}$ in times of strong turbulent dissipation ($t < 2\,\mathrm{h}$, $t \approx 4\,\mathrm{hours}$, $t \approx 5\,\mathrm{hours}$) and k^{-3} in times of weak dissipation ($t \approx 3.5\,\mathrm{hours}$, $t \approx 4.5\,\mathrm{hours}$, $t > 6\,\mathrm{hours}$).

At the end of the simulations (11.11 hours), the turbulence has died out and there is very little energy in the smaller scales. Notice that there is a wide variation in the spectra between 2.5-D ensemble members. Indeed after the first burst of turbulence the ensemble members begin to diverge in all three of the diagnostics presented. It is natural that such a long simulation of a highly nonlinear process like a breaking wave be sensitive to the addition of initial noise.

6.2. Case II: Statically stable IGW

The second case is a statically stable inertia-gravity wave, identical to the first case but with $a_0 = 0.86$. The Richardson number Ri_{IGW} in the wave solution (Eq. 9) is greater than 1/4, and the linear model has been used to verify that no exponentially growing normal mode solutions exist for any perturbation wavelength or orientation (not shown). As such, the primary perturbation analysis in this case involves calculating the leading singular vectors for a range of perturbation wavelengths and orientations. An optimization time of $\tau = 7.5$ minutes, chosen a posteriori, ensures that the primary and secondary singular vector analyses both yield a finite scale for the most amplified mode. The singular vector growth factors as functions of $\lambda_\parallel$ and α are shown in figure 2b. Again the leading parallel perturbation has shorter wavelength ($\lambda_\parallel = 0.638$ km) than the leading transverse perturbation ($\lambda_\parallel = 2.115$ km) and a larger growth factor, but only slightly so.

Figure 2e shows the energy density as a function of ϕ in the initial condition for the 2.5-D nonlinear simulations for the parallel and transverse singular vectors. Again the transverse perturbation is less focussed near the level of lowest static stability in the original wave. The amplitude A_1 of the initial perturbation was chosen such that the maximum energy density in the perturbation is 10% that of the original wave. Unlike a normal mode, which in the linear regime has a fixed spatial structure as its amplitude grows and oscillates, the structure of a singular vector changes with time (since its constituent normal modes each have a different decay rate and frequency). The choice of initial amplitude is therefore more consequential here in that it affects the spatial structure of the solution at the moment when nonlinear effects become important. Figure 2h shows the amplitude as a function of time for the 2.5-D simulations initialized with the leading parallel and transverse singular vectors, including results for an ensemble of simulations further perturbed by small-amplitude noise at $t = 0$. The wave perturbed by the transverse singular vector decays more than the wave perturbed by the parallel singular vector. The breaking is modest in general in this case, as the original wave is statically and dynamically stable.

Again we chose the transverse perturbation for the rest of the analysis. Figure 9 shows the 7.5-minute growth factors for the leading secondary singular vectors as functions of perturbation wavelength $\lambda_\perp$. The most amplifying perturbation has wavelength $\lambda_\perp = 300$ m. Also shown (filled diamonds) are the growth factors of the trailing singular vectors for $\lambda_\perp = 300$ m and $\lambda_\perp = 1800$ m (where the growth factor curve reaches a local maximum), and the growth factors for $\lambda_\perp = \infty$ (dashed lines). In the right panel are shown the growth factors from ensembles of randomly initialized (with a $k^{-5/3}$ energy spectrum) linear integrations with a range of perturbation wavelengths. The ensemble mean of the latter also has peaks near $\lambda_\perp = 300$ m and $\lambda_\perp = 1800$ m, suggesting that the secondary singular vectors are representative of modes likely to emerge spontaneously. Figure 10 shows the spatial structure of the secondary singular vector with $\lambda_\perp = 300$ m at the initial and optimization times. Notice that the spatial scale in the $(x_\parallel, \zeta)$ plane roughly matches the wavelength (300 m) in the $y_\perp$ direction. This seems to be a generic feature of the early-time unstable modes [primary and secondary, see *Fruman and Achatz*, 2012].

As in the case of the unstable IGW, it is through interaction with the $V_\perp$ component of the basic state that the secondary singular vector is growing at the optimization time.

The initial condition for the 3-D DNS is composed of the original IGW ($\lambda = 3$ km), the leading 7.5-minute transverse primary singular vector ($\lambda_\parallel = 2.115$ km), and the leading 7.5-minute secondary singular vector ($\lambda_\perp = 300$ m). Simulations were run with average grid spacing $\Delta \approx 3$ m ("fine") and $\Delta \approx 4.2$ m ("coarse") (see centre column of table 3). The initial buoyancy field from the fine 3-D DNS is shown in figure 11a. Note that although the base wave is statically stable, due to the finite amplitude primary perturbation there is a region of static instability at the level of weakest stability in the base wave (as evidenced by the fold in the $b = -0.03$ ms^{-2} surface of the initial condition). The temporal development of the flow field is visualized in figure 11b-f by contours of streamwise-averaged buoyancy and kinetic energy dissipation ϵ_k. The perturbation grows during the first minutes and generates turbulence in the least stable part of the wave. The turbulence remains confined to this region and is dissipated quickly. The peak dissipation is reached at $t = 11$ min and after 40 min the turbulence has basically vanished. During this period of turbulent decay some overturning occurs in the most stable part of the wave, similar to the case of the unstable IGW. Here, however, the overturning is too weak to create a negative vertical buoyancy gradient and breaking. It is thus simply dissipated by molecular heat transport.

Figure 12 shows the evolution of the wave amplitude and total energy dissipation from the 3-D DNS and the ensemble of 2.5-D simulations. The decay (and partial rebound) of the wave amplitude is very similar in 3-D and 2.5-D, but the onset of turbulence and the associated energy dissipation occur earlier in 3-D. In the lower portion of the left panel of figure 12 is shown the maximum and mean perturbation energy density from a linear 2.5-D integration initialized with the primary singular vector. The mean energy in the singular vector is maximum at the optimization time and then decays. The drops in the maximum perturbation energy density from the linear integration approximately coincide in time with the rebounds of the IGW amplitude from the nonlinear simulations. The spatial distribution of the dissipation (figure 13) is very similar in 2.5-D and 3-D. The energy dissipation is strongly correlated with the region of $Ri < 1/4$ (bounded by the dark-grey contour), particularly in the upper half of the domain in the 2.5-D simulation.

The base wave in this case being stable, it is not surprising that the peak in global mean dissipation is weaker than in case I (compare figures 6 and 12). Nevertheless, the kinetic energy dissipation can be locally more intense during the early phase of the simulation (compare the colored contours in figures 5 and 11). This can be attributed to the difference between a primary normal mode, used in case I, and a primary singular vector with short optimization time, used in case II. The latter extracts maximum energy in the early phase of the simulation.

The Kolmogorov length as a function of time from the two 3-D DNS is plotted in figure 14a. In the fine simulation η is always larger than Δ/π (indicated by the horizontal line), so all turbulence scales are resolved. Although η is briefly below Δ/π in the coarse simulation, the results are almost indistinguishable from the fine simulation (compare the projection and dissipation diagnostics shown in figure 12), so the simulations are grid-converged.

6.3. Case III: Statically unstable HGW

The third and final test case is the statically unstable ($a_0 = 1.2$) high frequency gravity wave ($\Theta = 70°$, period 15 minutes, phase speed 3.3 ms^{-1}).

The five-minute growth factors of the leading normal modes for a range of wavelengths $\lambda_{\|}$ and orientation angles α are shown in figure 2c. The fastest growing normal mode overall is the leading transverse ($\alpha = 90°$) mode with $\lambda_{\|} = 2929$ m. The wavelength of maximum growth rate is not very sensitive in this case to the orientation of the perturbation, with the peak for most orientation angles near $\lambda_{\|} = 3$ km (which happens to be the wavelength of the original wave). The leading parallel ($\alpha = 0$) normal mode is an exception, having a shorter wavelength of $\lambda_{\|} = 1589$ m. Figure 2c is comparable to figure 5 of *Fritts et al.* [2013] showing growth rates computed using the Floquet theory method of *Lombard and Riley* [1996] for a HGW with $a_0 = 1.1$. For example the growth factor of the leading transverse normal modes ($\alpha = 90$, or $k_i = 0$ in their notation) exhibits multiple peaks with the largest growth factor for primary perturbation wavelength close to the wavelength of the original wave.

The energy density in the leading transverse and parallel normal modes and the wave amplitude decay in the respectively initialized 2.5-D simulations are shown in panels f and i of figure 2. The high frequency and significant horizontal gradients in the HGW make it less similar to a steady stratified shear flow than the IGW. It is not surprising then that the energy density in the leading normal modes is not as strongly correlated in space with the level of lowest static stability. Once again it is the longer-wavelength transverse normal mode that leads to the most profound breaking of the original wave. The HGW decays more completely and more vigorously than does the unstable IGW (cf. figure 2g); its amplitude is reduced to about 0.3 within 30 minutes.

The five-minute growth factors of the leading secondary singular vectors as functions of perturbation wavelength $\lambda_\perp$ are shown in figure 15. The basic state is the 2.5-D simulation initialized with the wave and the leading transverse primary normal mode. Also shown are the five-minute growth factors of randomly initialized integrations. There is no clear peak in either case, but the growth factor does not increase much beyond $\lambda_\perp = 3$ km. Figure 16 shows the structure of the secondary singular vector with $\lambda_\perp = 3$ km at the initial and optimization times. Notice that the singular vector apears to have "propagated" up through the domain. In fact it is the original wave (and hence the entire reference frame) that has propagated downward about one third of a wavelength. Notice also that unlike for the elliptically polarized IGW, the transverse velocity in the basic state ($U_\parallel$ in the twice-rotated reference frame) is initially about an order of magnitude weaker than the parallel ($V_\perp$) component but at the optimization time it has grown due to interaction with the velocity shear in the HGW. *Achatz* [2007b] found that transverse primary perturbations to statically unstable HGW grow more through interaction with the shear in the wave than with the unstable buoyancy gradient.

The 3-D DNS was initialized with the original HGW ($\lambda = 3$ km), the leading transverse primary normal mode ($\lambda_\parallel = 2.929$ km) and the 5-minute secondary singular vector with $\lambda_\perp = 3$ km. Three simulations were performed, with grid spacing Δ of 1.9 m (fine resolution), 3.9 m (coarse 1) and 7.8 m (coarse 2). The initial buoyancy field from the fine resolution simulation is shown in figure 17 together with snapshots of the streamwise-averaged buoyancy and kinetic energy dissipation at a sequence of later times. The dissipation at early times is localized where the secondary singular vector energy is concentrated (cf. figure 16) but soon fills the domain. Comparisons of the amplitude decay and total energy dissipation are shown in figure 18. Both diagnostics are quite similar in 2.5-D and 3-D, although as in the previous cases the onset of turbulent dissipation occurs slightly earlier in 3-D. The distribution in space and time of the energy dissipation from the medium resolution (coarse 1) run is shown in figure 19. The regions of intense energy dissipation are approximately fixed in space (parallel to the heavy dashed black lines), particularly in the 2.5-D simulation.

Spanwise and streamwise averaged energy spectra from the 2.5-D ensemble and the medium (coarse 1) resolution 3-D DNS are plotted in figure 20 (computation of spectra for the fine simulation was too memory-intensive). Spectra from two times during the period of strong energy dissipation (15 and 30 minutes) and at the end of the simulation are shown. During the period of maximum turbulence, energy moves to smaller scales and close to a $k^{-5/3}$ spectrum forms. At the end of the simulation the spectrum has steepened as the energy in smaller scales has been lost to friction and thermal diffusion. The cascade of energy to the smallest scales is more efficient in the 3-D simulations, but the difference between the 2.5-D and 3-D spectra seems to be small in this case. Like in the intermediate-time spectra from case I (figure 8), the spectra at 90 minutes are close to the k^{-3} spectrum characteristic of anisotropic, buoyancy-dominated turbulence.

There is much less variation between ensemble members in the dissipation and spectra diagnostics than in the (much longer) unstable IGW simulations, and in the projection diagnostic there is much less variation relative to the amount of decay.

The Kolmogorov length η from the 3-D DNS with coarse, medium and fine resolution is plotted as a function of time in figure 14b. In the fine simulation η is always approximately equal to or larger than Δ/π (indicated by the horizontal lines) and can hence be considered fully resolved. Nevertheless, there is not much difference in terms of the wave amplitude and dissipation rates (figure 18) in the intense early phase (up to about 15 minutes) of the fine and coarse 1 simulations, so it is probably acceptable to use the latter for computing the spectra for figure 20. The coarse 2 simulation, on the other hand, has a slightly lower dissipation peak than the other two and is thus not quite resolving the smallest relevant scales.

7. Conclusion

A systematic but flexible method for constructing an efficient three-dimensional (3D) direct numerical simulation (DNS) of a breaking inertia-gravity wave has been presented. The method consists of four stages, which can be summarized as follows:

(1) Normal mode (NM) or singular vector (SV) analysis of the Boussinesq equations linearized about the inertia-gravity wave solution (Eq. 6). This entails a large number of 1-dimensional linear calculations in the once-rotated coordinate system (ξ, y, ζ).

(2) “2.5-dimensional” (2.5-D) nonlinear simulation of the full Boussinesq equations (Eq. 2) initialized with the inertia-gravity wave plus a leading NM or SV from step 1. These simulations are performed in the twice rotated coordinate system $(x_\parallel, y_\perp, \zeta)$ and are supplemented by ensembles of simulations with additional small-amplitude initial noise.

(3) SV analysis on the full equations linearized about the particular time-dependent 2.5-D solution from step 2 that resulted in the greatest reduction in the gravity-wave amplitude (using Eq. 13)

(4) 3-D DNS initialized with the inertia-gravity wave, the leading NM or SV from step 1 and a leading secondary SV from step 3. The dimensions of the integration domain are equal to the wavelengths of the wave and the leading perturbations.

The characteristics of the initial wave are completely determined by the atmosphere parameters N and f and the wavelength and propagation angle Θ of the wave (see tables 1 and 2). The primary instability structures (NM or SV) further depend on the viscosity ν and diffusivity μ and are characterized by the orientation angle α and wavelength $\lambda_{\parallel}$, and in the case of the singular vector the optimization time τ. The secondary singular vectors are characterized by their wavelength $\lambda_{\perp}$ and the optimization time, which may or may not be the same as that used for computing the primary singular vector.

The method has been applied to three test cases, resulting in the following initial conditions for the 3-D DNS:

(I) A statically unstable inertia-gravity wave (IGW) with wavelength $\lambda = 3$ km, propagation angle $\Theta = 89.5°$ (period 8 hours, phase speed 0.1 ms^{-1}), and amplitude $a_0 = 1.2$ (streamwise velocity amplitude $\Delta u_{\xi} = 14.6$ ms^{-1}) perturbed by the leading transverse primary normal mode with $\lambda_{\parallel} = 3.9$ km and the leading 5-minute secondary singular vector with $\lambda_{\perp} = 400$ m.

(II) A statically stable IGW with parameters identical to case I except the amplitude $a_0 = 0.86$ ($\Delta u_{\xi} = 10.4$ ms^{-1}), perturbed by the leading 7.5-minute transverse primary singular vector with $\lambda_{\parallel} = 2.115$ km and the leading 7.5-minute secondary singular vector with $\lambda_{\perp} = 300$ m.

(III) A statically unstable high-frequency gravity wave (HGW) with wavelength $\lambda = 3$ km, propagation angle $\Theta = 70°$ (period 15 minutes, phase speed 3.3 ms^{-1}) and amplitude

$a_0 = 1.2$ ($\Delta u_\xi = 12.2$ ms^{-1}) perturbed by the leading transverse normal mode with $\lambda_\| = 2.9$ km and the leading secondary singular vector with $\lambda_\perp = 3$ km.

The breaking of the unstable IGW [case I, also discussed in *Remmler et al.*, 2013] was perhaps the richest of the three cases. The turbulence and wave decay was intermittent and persisted for almost the period of the wave (8 hours). The preliminary linear instability analysis and nonlinear 2.5-D simulations indicated that this case could be treated in a domain relatively narrow in the $y_\perp$ direction, making such a long integration possible. After the first approximately 30 minutes, most of the energy dissipation in the 3-D simulation occurred near the level of static instability in the original wave, while in 2.5-D there is significant energy dissipation also in the stable part of the wave. In general it was the only case with significant differences between the 2.5-D and 3-D DNS and with significant variation between members of the ensemble in 2.5-D.

The unstable HGW (case III) resulted in a rapid and almost total breakdown of the wave, its amplitude decaying to about 30% of the threshold amplitude for static instability within just over a single wave period (15 minutes). The breaking of this wave seems to be relatively isotropic, with scales in all three directions comparable to the wavelength of the original wave, and the dissipation occurs in one powerful burst (as opposed to being intermittent) and does not appear to be very spatially correlated with the distributions of velocity and buoyancy in the original wave. The results of this test case were similar to those of *Fritts et al.* [2009a, b]. Although those authors did not include the Coriolis force in their calculations, it plays almost no role in the dynamics of high-frequency waves.

Probably the least interesting of the three cases (from the point of view of wave breaking) was the statically stable IGW (case II). The wave amplitude is reduced by about 5%, from

$a_0 = 0.86$ to about $|a| = 0.82$ before rebounding slightly after the optimization time of the primary singular vector (at which time its energy – in the linear solution – begins to decrease). *Achatz* [2007a] discussed a similar case (but for a wave with 6 km wavelength) and found that perturbation by a primary SV with ten times larger relative amplitude than that considered here could lead, in nonlinear simulations, to significant reduction in the amplitude of the IGW. Such a large perturbation, however, makes the initial condition locally approach or exceed the static instability threshold.

Overall the results of the 2.5-D simulations are remarkably similar to those of the 3-D DNS in terms of the projection and resolved-energy dissipation diagnostics. The initial phase of wave breaking tends to be more rapid and more intense in the 3-D simulations – understandable since it provides more degrees of freedom and avenues to exchange energy between spatial scales. The spatial and temporal distribution of the energy dissipation are similar.

A possible objection to the approach advocated here is that the computational domain and initial condition are too carefully chosen for the results to be relevant to a wave breaking spontaneously in nature. For that reason, *Remmler et al.* [2013] performed additional simulations with the inertia-gravity wave from case I, in domains half as wide (200 m) and twice as wide (800 m) in the $y_\perp$ direction and with small amplitude noise instead of the secondary singular vector. It was found that the breaking of the wave in the narrow domain was more like in the 2.5-D simulations, while the breaking in the wider domain was more like the optimally initialized 3-D DNS, suggesting that the optimal initialization might be a closer approximation to nature than a randomly initialized simulation in a bounded domain. Since the breaking of the HGW (case III) was so similar in 2.5-D and in 3-D, this test was not deemed necessary.

While simulation of realistic breaking waves in the upper mesosphere is becoming tractable with improved computing technology, it remains an expensive and time-consuming undertaking and is still out of reach for waves in the ocean and most of the atmosphere. For that one must rely on large-eddy simulation (LES) models. An immediate application of the results presented here is in the validation of LES schemes against a reliable properly resolved solution. The LES can then serve as an essential intermediate tool for the testing of gravity-wave drag parameterizations, which are needed by every weather-forecast and climate model, or simply for extending the parameter range (higher Reynolds numbers, larger simulation domains) that can be explored in monochromatic wave-breaking studies of the type presented here. We would be happy to share the data from the 3-D DNS with other researchers. Summaries of the data will be made available on the World Wide Web.

Appendix A: Normal Modes and Singular Vectors

Consider a system of coupled linear ordinary differential equations

$$\frac{\mathrm{d}}{\mathrm{d}t}\mathbf{x} = \mathsf{A}\mathbf{x}, \tag{A1}$$

where $\mathbf{x}$ is a vector and A is a matrix which may depend on time. In the context of the primary instability analysis (section 3.1), $\mathbf{x}$ consists of the real and imaginary parts of the perturbation velocity and buoyancy amplitudes at a discrete set of ϕ values (where $\phi \in (0, 2\pi)$ is the phase of the original gravity wave) and A depends on ϕ through the basic state fields but is independent of time. For the secondary instability analysis (section 3.2), $\mathbf{x}$ consists of the same fields at discrete points on the $(x_\parallel, \phi)$ grid and A is time dependent.

The *normal modes* of (A1) are solutions of the form

$$\mathbf{x}(t) = \mathbf{x}_0 e^{\gamma t}, \tag{A2}$$

where $\mathbf{x}_0$ is an eigenvector of A and γ the corresponding eigenvalue. The *leading* normal mode is the one with the largest *growth rate* (the real part of γ). In general A is a very large matrix, and one is interested only in the fastest growing normal modes, so it is convenient to use an iterative eigenvector solution method like the Arnoldi method, but these methods find the eigenvalue with the largest magnitude rather than the eigenvalue with the largest real part. The answer is to instead find the eigenvalues of the propagator matrix Φ_τ, defined by

$$\mathbf{x}(\tau) = \Phi_\tau \mathbf{x}(0). \tag{A3}$$

When A is time independent, $\Phi_\tau \equiv \exp(\tau\mathsf{A})$ and has the same eigenvectors as A and eigenvalues of the form $\Gamma = \exp(\gamma\tau)$. Since $|\Gamma| = \exp(\mathrm{Re}(\gamma)t)$, the eigenvalues of Φ_τ with the largest magnitude correspond to the eigenvalues of A with the largest real part. Note that the matrix Φ_τ need not be known explicitly in order to calculate its eigenvalues and eigenvectors using a tool such as the ARPACK library [*Lehoucq et al.*, 1998]. One need only have a way of calculating $\mathbf{x}(\tau)$ from $\mathbf{x}_0$, i.e. the linear model.

It is often required to find the initial perturbations $\mathbf{x}_0$ for which the *growth factor* after time τ,

$$\sigma \equiv \sqrt{\frac{\mathbf{x}(\tau)^\dagger \mathsf{M} \mathbf{x}(\tau)}{\mathbf{x}_0^\dagger \mathsf{M} \mathbf{x}_0}} = \sqrt{\frac{\mathbf{x}_0^\dagger \Phi_\tau^\dagger \mathsf{M} \Phi_\tau \mathbf{x}_0}{\mathbf{x}_0^\dagger \mathsf{M} \mathbf{x}_0}} \tag{A4}$$

is maximized. Here M is a positive-definite matrix which defines a norm (such as the total energy) and its associated inner product, and $\mathbf{x}^\dagger$ is the conjugate-transpose of $\mathbf{x}$. It can be shown that σ is maximized when $\mathbf{x}_0$ is the eigenvector of the matrix $\mathsf{M}^{-1}\Phi_\tau^\dagger\mathsf{M}\Phi_\tau$ with the largest (in magnitude) eigenvalue. The eigenvectors $\{\mathbf{x}_k\}$ of $\mathsf{M}^{-1}\Phi_\tau^\dagger\mathsf{M}\Phi_\tau$ are called the *singular vectors* of the system described by A with respect to the optimization time τ.

It is simpler to find the vectors $\mathbf{q}_k = \mathsf{N}\mathbf{x}_k$, where $\mathsf{M} = \mathsf{N}^\dagger\mathsf{N}$ is the Cholesky factorization of M, because the $\mathbf{q}_k$ satisfy the Hermitian eigenvector equation

$$(\mathsf{N}\Phi_\tau\mathsf{N}^{-1})^\dagger(\mathsf{N}\Phi_\tau\mathsf{N}^{-1})\mathbf{q}_k = \sigma^2\mathbf{q}_k. \tag{A5}$$

The singular vectors $\mathbf{x}_k$ can then be recovered by computing $\mathbf{x}_k = \mathsf{N}^{-1}\mathbf{q}_k$. In order to calculate the $\mathbf{q}_k$, both the linear model – to compute $\mathbf{y} = \Phi_\tau\mathbf{x}$ – and its *adjoint* – to compute $\Phi_\tau^\dagger\mathbf{y}$ – are required. In the present study, the adjoint models were constructed using the tool TAMC [*Giering and Kaminski*, 1998].

When A is time-dependent (such as in the calculation of the secondary instabilities), the normal mode problem is not well-defined, but singular vectors can be calculated for any linear system. Furthermore, since the vectors $\mathbf{q}_k$ are the eigenvectors of a positive definite, Hermitian matrix, they form an orthonormal set. It follows that the singular vectors $\mathbf{x}_k$ are orthonormal with respect to the norm M. It is easily shown that they are orthogonal also at the optimization time τ, i.e.

$$(\Phi_\tau\mathbf{x}_j)^\dagger\mathsf{M}(\Phi_\tau\mathbf{x}_k) = \mathbf{x}_j^\dagger\Phi_\tau^\dagger\mathsf{M}\Phi_\tau\mathbf{x}_k = \sigma_k^2\mathbf{x}_j^\dagger\mathsf{M}\mathbf{x}_k = \delta_{jk}\sigma_k^2. \tag{A6}$$

Appendix B: Projection onto Free Gravity Waves

An important diagnostic quantity for simulations of the breaking of a inertia-gravity wave is the projection of the solution onto the inertia-gravity wave as a function of time.

See the appendix of *Achatz* [2007b] for the more general problem of projecting the solution onto all free inertia-gravity waves and vortical modes.

The projection onto just the original inertia-gravity wave may be extracted from the streamwise-spanwise mean fields $\overline{u}_\parallel$, $\overline{v}_\perp$, $\overline{w}_\zeta$ and $\overline{b}$, where for the quantity X,

$$\overline{X}(\phi, t) = \frac{1}{\lambda_\parallel \lambda_\perp} \int_0^{\lambda_\perp} \int_0^{\lambda_\parallel} X(x_\parallel, y_\perp, \phi, t) \mathrm{d}x_\parallel \mathrm{d}y_\perp. \tag{B1}$$

The free linear modes depending only on ζ and t and periodic in ζ with period λ consist of the geostrophically balanced vortical modes

$$\begin{aligned} V_n &\equiv [\overline{u}_\parallel, \overline{v}_\perp, \overline{w}_\zeta, \overline{b}]_n^0 \\ &\equiv \frac{\sqrt{2}N}{\sqrt{N^2 \cos^2\Theta + f^2 \sin^2\Theta}} \left[\cos\Theta \sin\alpha, \cos\Theta\cos\alpha, 0, f\sin\Theta\right] \exp\left(inK\zeta\right), \end{aligned} \tag{B2}$$

and the upward and downward propagating inertia-gravity waves

$$\begin{aligned} G_n^\pm &\equiv [\overline{u}_\parallel, \overline{v}_\perp, \overline{w}_\zeta, \overline{b}]_n^\pm \\ &\equiv \left[i\cos\alpha + \frac{f\sin\Theta}{\omega^\pm}\sin\alpha, -i\sin\alpha + \frac{f\sin\Theta}{\omega^\pm}\cos\alpha, 0, -\frac{N^2\cos\Theta}{\omega^\pm}\right] \exp\left[i\left(nK\zeta - \omega^\pm t\right)\right]. \end{aligned} \tag{B3}$$

Here Θ is the angle of phase propagation of the original wave, α is the orientation of the primary perturbation, n is an integer, and

$$\omega^\pm = \pm\sqrt{f^2\sin^2\Theta + N^2\cos^2\Theta}. \tag{B4}$$

In addition there is the "mode" $W \equiv [\overline{u}_\parallel, \overline{v}_\perp, \overline{w}_\zeta, \overline{b}]^w = [0, 0, \sqrt{2}, 0]$ representing the streamwise and spanwise mean of w_ζ (it follows from the continuity equation averaged over $x_\parallel$ and $y_\perp$ that $\overline{w}_\zeta$ is independent of ζ).

It is readily shown that the set $\{V_n^0, G_n^+, G_n^-, W\}$, where $n = 1, 2, 3, \ldots$, forms an orthonormal basis in the energy norm

$$||[\overline{u}_\parallel, \overline{v}_\perp, \overline{w}_\zeta, \overline{b}]||^2 \equiv \frac{1}{2\lambda} \int_0^\lambda \left(|\overline{u}_\parallel|^2 + |\overline{v}_\perp|^2 + |\overline{w}_\zeta|^2 + \frac{|b|^2}{N^2}\right) \mathrm{d}\zeta \tag{B5}$$

for periodic functions of ζ with period λ. The original inertia-gravity wave, which had upward vertical group speed and therefore downward vertical phase speed, is the mode G_1^-.

Defining the discrete Fourier Transform according to

$$\hat{X}_j = \frac{1}{N_\zeta} \sum_{l=1}^{N_\zeta} \overline{X}_l \exp\left(-i\frac{2\pi j l}{N_\zeta}\right), \tag{B6}$$

where N_ζ is the number of grid points in the ζ direction, the (complex) amplitude of the inertia-gravity wave at a given time is then the scalar product of the transformed discrete fields with G_1^-:

$$\begin{aligned} A(t) &= \frac{1}{2}\left(\hat{u}_{\parallel 1}^{\,*}\hat{u}_{\parallel 1}^{\,-} + \hat{v}_{\perp 1}^{\,*}\hat{v}_{\perp 1}^{\,-} + \frac{1}{N^2}\hat{b}_1^*\hat{b}_1^-\right) \\ &= \frac{1}{2}\left[\left(i\cos\alpha + \frac{f\sin\Theta}{\omega^-}\sin\alpha\right)\hat{u}_{\parallel 1}^{\,*} + \left(-i\sin\alpha + \frac{f\sin\Theta}{\omega^-}\cos\alpha\right)\hat{v}_{\perp 1}^{\,*} - \frac{N^2\cos\Theta}{\omega^-}\hat{b}_1^*\right], \end{aligned} \tag{B7}$$

where $[\hat{u}_{\parallel 1}^{\,-}, \hat{v}_{\perp 1}^{\,-}, 0, \hat{b}_1^-]$ is the complex amplitude of the mode G_1^- (from Eq. B3). The magnitude of the amplitude normalized relative to the threshold for static instability $|\hat{b}_C| = N^2/(K\cos\Theta)$ is then

$$|a(t)| = \frac{|\hat{b}_1^-|}{|\hat{b}_C|}|A(t)| = \frac{2\cos\Theta\sin\Theta}{(\lambda/2\pi)|\omega^-|}|A(t)|. \tag{B8}$$

Appendix C: Computational resources used for the 3-D DNS

The 3-D direct numerical simulations for the three test cases were performed at different high-performance computing centres.

For the unstable IGW, a resolution of $\Delta = 3$ m and therefore 172.8 million grid cells were required for the solution to be fully resolved. The simulation was run on the NEC SX-9 vector computer at HLRS in Stuttgart, Germany. A single node of this machine (500 GB memory, 16 vector processors with 100 GFLOP/s peak performance each) had sufficient memory to store the complete flow field. Hence we could avoid domain decomposition and relied on shared memory parallelization only. The efficient Poisson solver employs a discrete Fourier Transform in one direction in combination with a Bi-Conjugate Gradient Stabilized (BiCGSTAB) solver [*van der Vorst*, 1992] in the plane perpendicular to the chosen direction. The Fourier Transform converts the three-dimensional problem into a set of independent two-dimensional problems, which are solved in parallel. The simulation of a flow time of 35 000 s (270 000 time steps) required a *wall time* of 1100 hours, which corresponds to 85.7×10^{-9} node-seconds per time step and cell.

The simulations of the stable IGW were carried out on the LOEWE cluster at CSC Frankfurt, Germany. This machine consists of nodes with two AMD Opteron 6172 CPUs (12 cores per CPU, 8.4 GFlop/s per core peak performance) and 64 GB memory. The fully resolved DNS with 71 million grid cells was decomposed into 192 blocks and simulated on eight nodes. The integration up to $t = 100$ min (38 600 time steps) took 183 hours, i.e. 1.93×10^{-6} node-seconds per time step and cell.

The simulations of the unstable HGW were the most demanding and were run on the Cray XE6 cluster at HLRS Stuttgart, consisting of nodes with two AMD Opteron 6276 (Interlagos) CPUs (16 cores per CPU, 9.2 GFlop/s per core peak performance) and 32 GB memory. The fully resolved DNS with 3624 million grid cells was decomposed into 4096 blocks and simulated on 512 nodes using 8 processor cores per node. The integration up to $t = 46.2$ min (49 460 time steps) required a wall time of about 288 hours. Hence the computational performance was 2.96×10^{-6} node-seconds per time step and cell.

Acknowledgments. U.A. and S.H. thank the German Research Foundation (Deutsche Forschungsgemeinschaft, DFG) for partial support through the MetStröm (Multiple Scales in Fluid Mechanics and Meteorology) Priority Research Program (SPP 1276), and through Grants HI 1273/1-2 and Ac71/4-2. Computational resources were provided by the HLRS Stuttgart under the grants TIGRA and DINSGRAW and by the LOEWE-CSC Frankfurt. Data from the simulations are available on request from the authors.

References

Achatz, U. (2005), On the role of optimal perturbations in the instability of monochromatic gravity waves, *Phys. Fluids*, *17*, 1–27.

Achatz, U. (2007a), The primary nonlinear dynamics of modal and nonmodal perturbations of monochromatic inertia-gravity waves, *J. Atmos. Sci.*, *64*, 74–95.

Achatz, U. (2007b), Modal and nonmodal perturbations of monochromatic high-frequency gravity waves: primary nonlinear dynamics, *J. Atmos. Sci.*, *64*, 1977–1994.

Andreassen, O., C. E. Wasberg, D. C. Fritts, and J. R. Isler (1994), Gravity wave breaking in two and three dimensions 1. Model description and comparison of two-dimensional evolutions, *J. Geophys. Res.*, *99*, 8095–8108.

Baldwin, M. P., L. J. Gray, T. J. Dunkerton, K. Hamilton, P. H. Haynes, W. J. Randel, J. R. Holton, M. J. Alexander, I. Hirota, T. Horinouchi, D. B. A. Jones, J. S. Kinnersley, C. Marquardt, K. Sato, and M. Takahashi (2001), The Quasi-Biennial Oscillation, *Rev. Geophys.*, *39*, 179–229.

Brethouwer, G., P. Billant, E. Lindborg, and J. M. Chomaz (2007), Scaling analysis and simulation of strongly stratified turbulent flows, *J. Fluid Mech.*, *585*, 343–368.

Carnevale, F. G., M. Briscolini, and P. Orlandi (2001), Buoyancy to inertial range transition in forced stratified turbulence, *J. Fluid Mech.*, *427*, 205–239.

Chun, H. Y., M. D. Song, J. W. Kim, and J. J. Baik (2001), Effects of gravity wave drag induced by cumulus convection on the atmospheric general circulation, *J. Atmos. Sci.*, *58*, 302–319.

Cot, C. (2001), Equatorial mesoscale wind and temperature fluctuations in the lower atmosphere, *J. Geophys. Res.*, *106*, 1523–1532.

Durran, D. R. (2010), *Numerical Methods for Fluid Dynamics*, 516pp. pp., Springer, New York.

Farrell, B. F., and P. J. Ioannou (1996a), Generalized stability theory. Part I: Autonomous operators, *J. Atmos. Sci.*, *53*, 2025–2040.

Farrell, B. F., and P. J. Ioannou (1996b), Generalized stability theory. Part II: Nonautonomous operators, *J. Atmos. Sci.*, *53*, 2041–2053.

Fritts, D. C., and M. J. Alexander (2003), Gravity wave dynamics and effects in the middle atmosphere, *Rev. Geophys.*, *41*, 3.1–3.64.

Fritts, D. C., and L. Wang (2013), Gravity wave-fine structure interactions. Part II: Energy dissipation evolutions, statistics, and implications, *J. Atmos. Sci.*, *70*, 3735–3755.

Fritts, D. C., L. Wang, J. Werne, T. Lund, and K. Wan (2009a), Gravity wave instability dynamics at high Reynolds numbers. Part I: Wave field evolution at large amplitudes and high frequencies, *J. Atmos. Sci.*, *66*, 1126–1148.

Fritts, D. C., L. Wang, J. Werne, T. Lund, and K. Wan (2009b), Gravity wave instability dynamics at high Reynolds numbers. Part II: Turbulence evolution, structure, and anisotropy, *J. Atmos. Sci.*, *66*, 1149–1171.

Fritts, D. C., L. Wang, and J. A. Werne (2013), Gravity wave-fine structure interactions. Part I: Influences of fine structure form and orientation on flow evolution and instability, *J. Atmos. Sci.*, *70*, 3710–3734.

Fruman, M. D., and U. Achatz (2012), Secondary instabilities in breaking inertia-gravity waves, *J. Atmos. Sci.*, *69*, 303–322.

Giering, R., and T. Kaminski (1998), Recipes for adjoint code construction, *ACM Trans. Math. Software*, *24*, 437–474.

Grimsdell, A. W., M. J. Alexander, P. T. May, and L. Hoffmann (2010), Waves generated by convection with direct validation via satellite, *J. Atmos. Sci.*, *67*, 1617–1631.

Hines, C. O. (1965), Dynamical heating of the upper atmosphere, *J. Geophys. Res.*, *70*, 177–183.

Hines, C. O. (1997), Doppler-spread parameterization of gravity-wave momentum deposition in the middle atmosphere. Part I: Basic formulation, *J. Atmos. Sol.-Terr. Phys.*, *59*, 371–386.

Howard, L. N. (1961), Note on a paper of John W. Miles, *J. Fluid Mech.*, *10*, 509–512.

Kim, Y.-J., S. D. Eckermann, and H.-Y. Chun (2003), An overview of the past, present and future ofgravity-wave drag parameterization for numerical climateand weather prediction models, *Atmosphere-Ocean*, *41*(1), 65–98.

Klaassen, G. P., and W. R. Peltier (1985), The onset of turbulence in finite-amplitude Kelvin-Helmholtz billows, *J. Fluid Mech.*, *155*, 1–35.

Kraichnan, R. H., and D. Montgomery (1980), Two-dimensional turbulence, *Rep. Prog. Phys.*, *43*, 547–619.

Lehoucq, R. B., D. C. Sorensen, and C. Yang (1998), *ARPACK Users' Guide: Solution of large-scale eigenvalue problems with implicitly restarted Arnoldi methods.*, 160 pp., SIAM.

Lelong, M.-P., and T. J. Dunkerton (1998), Inertia-gravity wave breaking in three dimensions. Part I: Convectively stable waves, *J. Atmos. Sci.*, *55*, 2473–2488.

Lilly, D. K., J. M. Nicholls, R. M. Chervin, P. J. Kennedy, and J. B. Klemp (1982), Aircraft measurements of wave momentum flux over the Colorado Rocky Mountains, *Q.J.R.M.S.*, *108*, 625–642.

Lindzen, R. S. (1973), Wave-mean flow interactions in the upper atmosphere, *Bound.-Lay. Meteorol.*, *4*, 327–343.

Lindzen, R. S. (1981), Turbulence and stress owing to gravity wave and tidal breakdown, *J. Geophys. Res.*, *86*, 9707–9714.

Liu, W., F. P. Bretherton, Z. Liu, L. Smith, H. Lu, and C. J. Rutland (2010), Breaking of progressive internal gravity waves: Convective instability and shear instability, *J. Phys. Oceanogr.*, *40*, 2243–2263.

Lombard, P. N., and J. J. Riley (1996), Instability and breakdown of internal gravity waves. I. Linear stability analysis, *Phys. Fluids*, *8*, 3271–3287.

Lund, T. S., and D. C. Fritts (2012), Numerical simulation of gravity wave breaking in the lower thermosphere, *J. Geophys. Res.*, *117*, D21105.

McFarlane, N. (1987), The effect of orographically excited gravity wave drag on the general circulation of the lower stratosphere and troposphere, *J. Atmos. Sci.*, *44*, 1775–1800.

McLandress, C. (1998), On the importance of gravity waves in the middle atmosphere and their parameterization in general circulation models, *J. Atmos. Sol.-Terr. Phy.*, *60*, 1357–1383.

Miles, J. W. (1961), On the stability of heterogeneous shear flows, *J. Fluid Mech.*, *10*, 496–508.

NOAA, US Air Force, and US Air (1976), US Standard Atmosphere, 1976, *Tech. rep.*, NOAA-S/T.

O'Sullivan, D., and T. J. Dunkerton (1995), Generation of inertia-gravity waves in a simulated life cycle of baroclinic instability, *J. Atmos. Sci.*, *52*, 3695–3716.

Plougonven, R., and C. Snyder (2007), Inertia-gravity waves spontaneously generated by jets and fronts. Part I: Different baroclinic life cycles, *J. Atmos. Sci.*, *64*, 2502–2520.

Remmler, S., and S. Hickel (2012), Direct and large eddy simulation of stratified turbulence, *Intl. J. Heat Fluid Flow*, *35*, 13–24.

Remmler, S., and S. Hickel (2013), Spectral structure of stratified turbulence: Direct numerical simulation and predictions by LES, *Theor. Comput. Fluid Dyn.*, *27*, 319–336.

Remmler, S., M. D. Fruman, and S. Hickel (2013), Direct numerical simulation of a breaking inertia-gravity wave, *J. Fluid Mech.*, *722*, 424–436.

Shu, C.-W. (1988), Total-variation-diminishing time discretizations, *SIAM J. Sci. Stat. Comput.*, *9(6)*, 1073–1084.

Smith, R. B. (1979), The influence of mountains on the atmosphere, *Adv. Geophys.*, *21*, 87–230.

Vallis, G. K. (2006), *Atmospheric and oceanic fluid dynamics*, Cambridge University Press.

van der Vorst, H. A. (1992), Bi-CGSTAB: A fast and smoothly converging variant of Bi-CG for the solution of nonsymmetric linear systems, *SIAM J. Sci. Stat. Comput.*, *13*(2), 631–644.

Williamson, J. H. (1980), Low-storage Runge–Kutta schemes, *J. Comput. Phys.*, *35*(1), 48–56.

Yamazaki, Y., T. Ishihara, and Y. Kaneda (2002), Effects of wavenumber truncation on high-resolution direct numerical simulation of turbulence, *J. Phys. Soc. Jpn.*, *71*, 777–781.

Kinematic viscosity	ν	$1\ \mathrm{m^2 s^{-1}}$
Thermal diffusivity	μ	$1\ \mathrm{m^2 s^{-1}}$
Latitude for Coriolis parameter	ϕ_C	70 N
Coriolis parameter	f	$1.37 \times 10^{-4}\ \mathrm{s^{-1}}$
Brunt-Väisälä frequency	N	$2 \times 10^{-2}\ \mathrm{s^{-1}}$
Acceleration due to gravity	g	$9.81\ \mathrm{ms^{-2}}$

Table 1. Atmosphere parameters.

Case		Amplitude	Propagation angle Θ	Primary perturbation	Secondary perturbation
I.	Unstable IGW	$a_0 = 1.2$ $\Delta u_\xi = 14.6\ \mathrm{ms^{-1}}$ $\Delta b = 0.23\ \mathrm{ms^{-2}}$	89.5°	NM, $\alpha = 90°$ $\lambda_\parallel = 3.98$ km $A_1 = 0.05$	$\lambda_\perp = 0.4$ km $A_2 = 0.02$
II.	Stable IGW	$a_0 = 0.86$ $\Delta u_\xi = 10.4\ \mathrm{ms^{-1}}$ $\Delta b = 0.16\ \mathrm{ms^{-2}}$	89.5°	SV, $\alpha = 90°$ $\lambda_\parallel = 2.12$ km $A_1 = 0.1$	$\lambda_\perp = 0.3$ km $A_2 = 0.01$
III.	Unstable HGW	$a_0 = 1.2$ $\Delta u_\xi = 12.2\ \mathrm{ms^{-1}}$ $\Delta b = 0.24\ \mathrm{ms^{-2}}$	70°	NM, $\alpha = 90°$ $\lambda_\parallel = 2.93$ km $A_1 = 0.05$	$\lambda_\perp = 3.0$ km $A_2 = 0.01$

Table 2. Parameters of the initial conditions for the 3-D DNS test cases. A_1 and A_2 are the amplitudes of the primary and secondary perturbations in terms of the maximum perturbation energy density compared to the maximum energy density in the basic state. Δu_ξ and Δb are the amplitudes of the u_ξ velocity component and buoyancy in the original wave.

	I. Unstable IGW	II. Stable IGW	III. Unstable HGW
PRIM. INSTAB.			
n_ϕ ($\Delta\zeta$)	1024 (3 m)	1024 (3 m)	1024 (3 m)
time step Δt	0.025 s	0.025 s	0.025 s
integration time τ	5 min	7.5 min	5 min
2.5-D DNS			
$n_{x_\parallel} \times n_\zeta$ ($\Delta x_\parallel$, $\Delta\zeta$)	660×500 (6 m, 6 m)	350×500 (6 m, 6 m)	500×500 (6 m, 6 m)
time step Δt	0.05 s	0.05 s	0.05 s
integration time τ	666 min	60 min	90 min
SECOND. INSTAB.			
$n_{x_\parallel} \times n_\phi$ ($\Delta x_\parallel$, $\Delta\zeta$)	128×512 (31 m, 6 m)	128×512 (17 m, 6 m)	256×256 (11 m, 12 m)
time step Δt	0.05 s	0.05 s	0.05 s
integration time τ	5 min	7.5 min	5 min
COARSE RES. 3-D DNS			
$n_{x_\parallel} \times n_{y_\perp} \times n_\zeta$	$640 \times 64 \times 500$	$512 \times 64 \times 768$	768^3 / 384^3
cell size Δ	6.2 m, 6.3 m, 6.0 m	4.1 m, 4.7 m, 3.9 m	3.9 m / 7.8 m
integration time τ	1000 min	100 min	91 min / 157 min
FULL RES. 3-D DNS			
$n_{x_\parallel} \times n_{y_\perp} \times n_\zeta$	$1350 \times 128 \times 1000$	$720 \times 96 \times 1024$	$1536 \times 1536 \times 1536$
cell size Δ	2.9 m, 3.1 m, 3.0 m	2.9 m, 3.1 m, 2.9 m	1.9 m
integration time τ	572 min	100 min	46 min

Table 3. Parameters of numerical calculations of primary and secondary instability growth factors and of 2.5-D and 3-D direct numerical simulations.

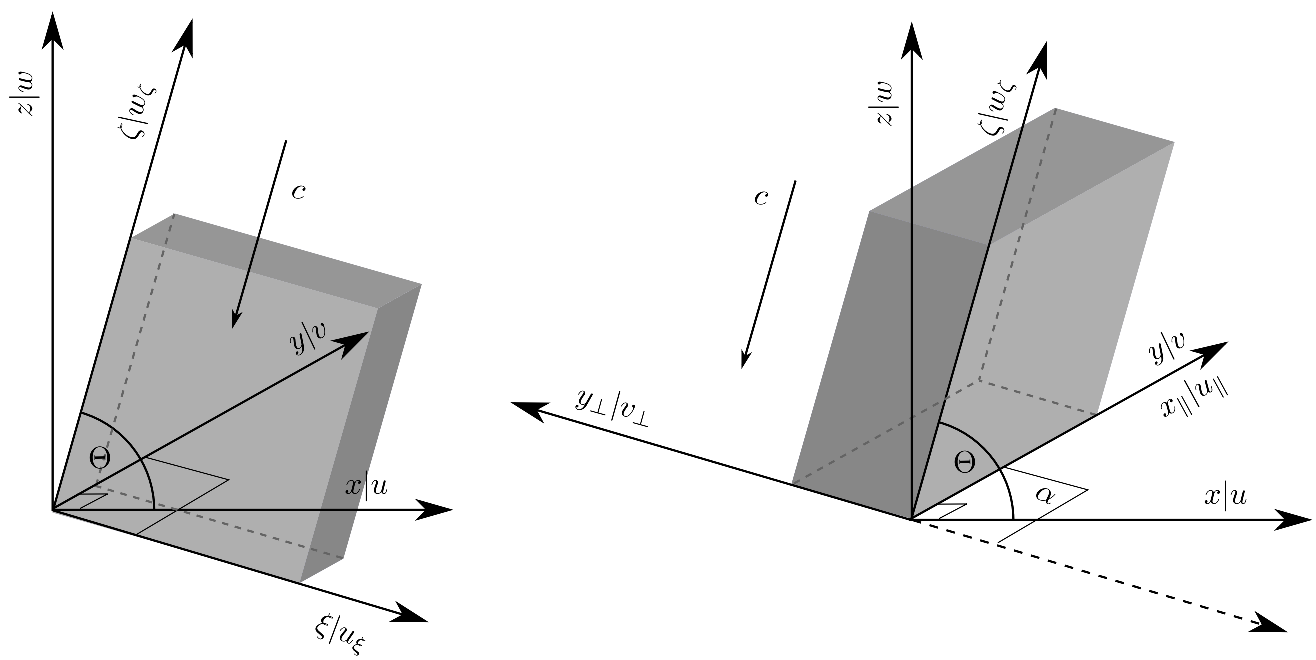

Figure 1. Rotated coordinate systems for primary and secondary instability analyses [after *Remmler et al.*, 2013].

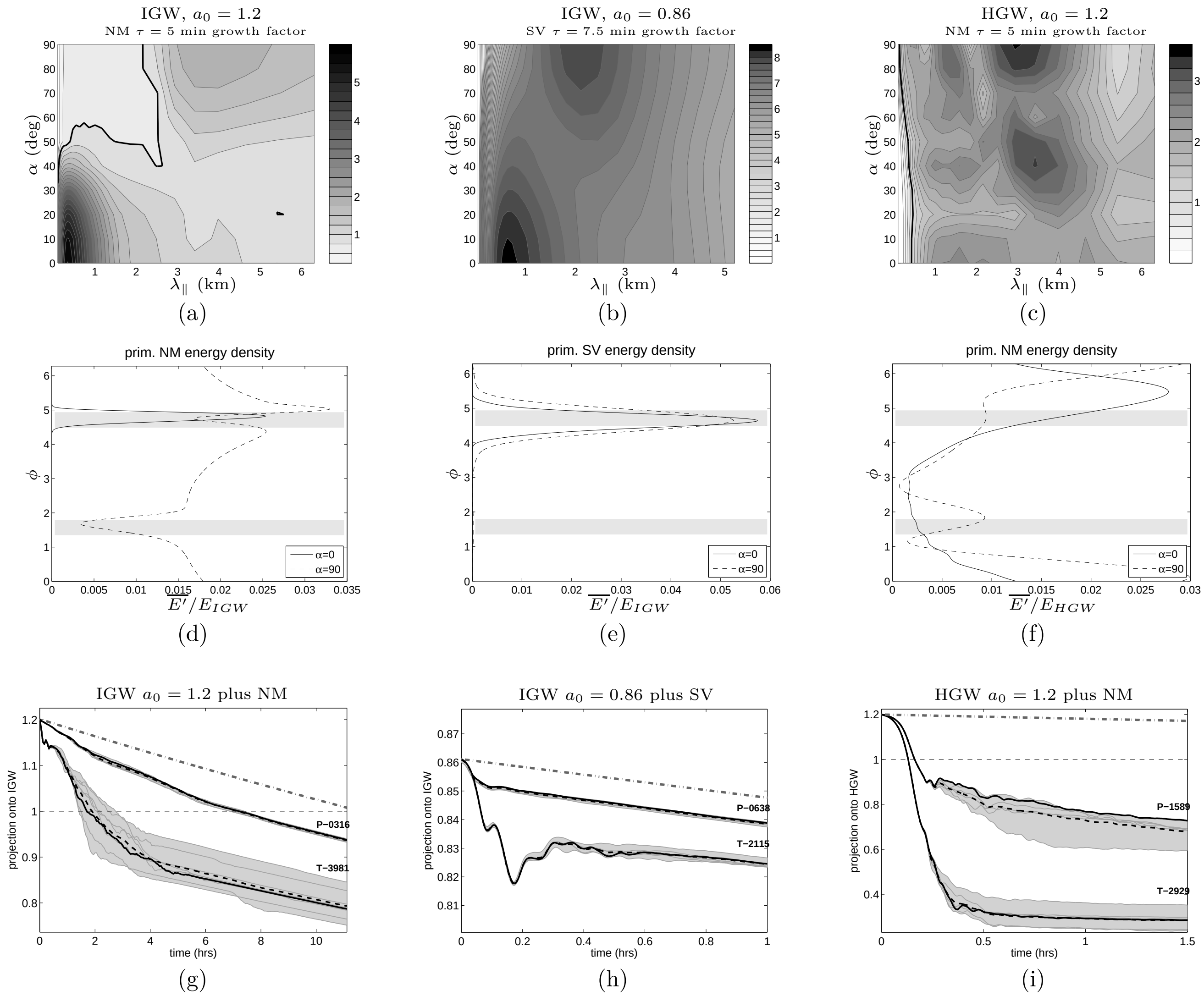

Figure 2. *Top row*: growth factors of leading primary linear modes as functions of perturbation wavelength and orientation angle: (a) normal modes of unstable IGW; (b) $\tau = 7.5$ min singular vectors of stable IGW; (c) normal modes of unstable HGW. *Middle row*: streamwise-spanwise mean perturbation energy density in initial condition of 2.5-D simulations, normalized by the mean energy density in the IGW (E_{IGW}) or HGW (E_{HGW}), for (d) leading transverse ($\alpha = 90°$) and parallel ($\alpha = 0$) NM of unstable IGW; (e) leading transverse and parallel SV of stable IGW; (f) leading transverse and parallel NM of unstable HGW. Shaded regions in panels (d)-(f) are for reference, indicating levels of maximum ($\phi = \pi/2$) and minimum ($\phi = 3\pi/2$) static stability in the basic state wave. *Bottom row*: time dependent projection of 2.5-D nonlinear solution onto the (g) unstable IGW; (h) stable IGW; (i) unstable HGW. Grey-shaded regions in panels (g)-(i) represent the range of values from integrations with additional small amplitude initial noise (ensemble average indicated by dashed lines) and dash-dot line represents the viscous decay of the unperturbed wave.

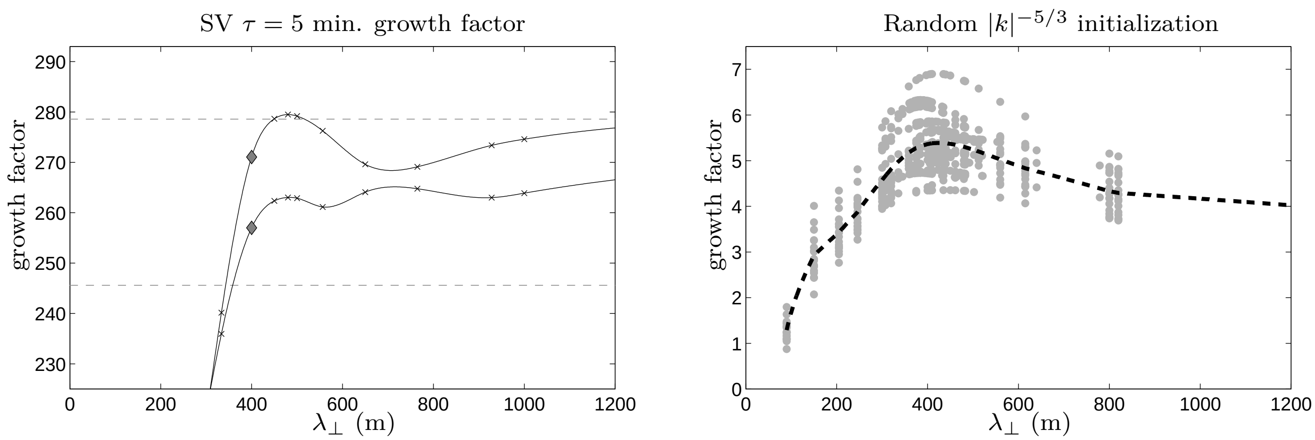

Figure 3. Linear growth factors of leading and second-leading 5-minute secondary singular vectors (*left*) and of randomly initialized perturbations (*right*) versus secondary perturbation wavelength $\lambda_\perp$ for the unstable IGW perturbed by its leading transverse primary normal mode. Dashed horizontal lines in left panel are growth factors of leading SV for $\lambda_\perp = \infty$; filled diamonds indicate growth factors at $\lambda_\perp = 400$ m. Heavy dashed line in right panel represents ensemble-mean growth factor at each wavelength.

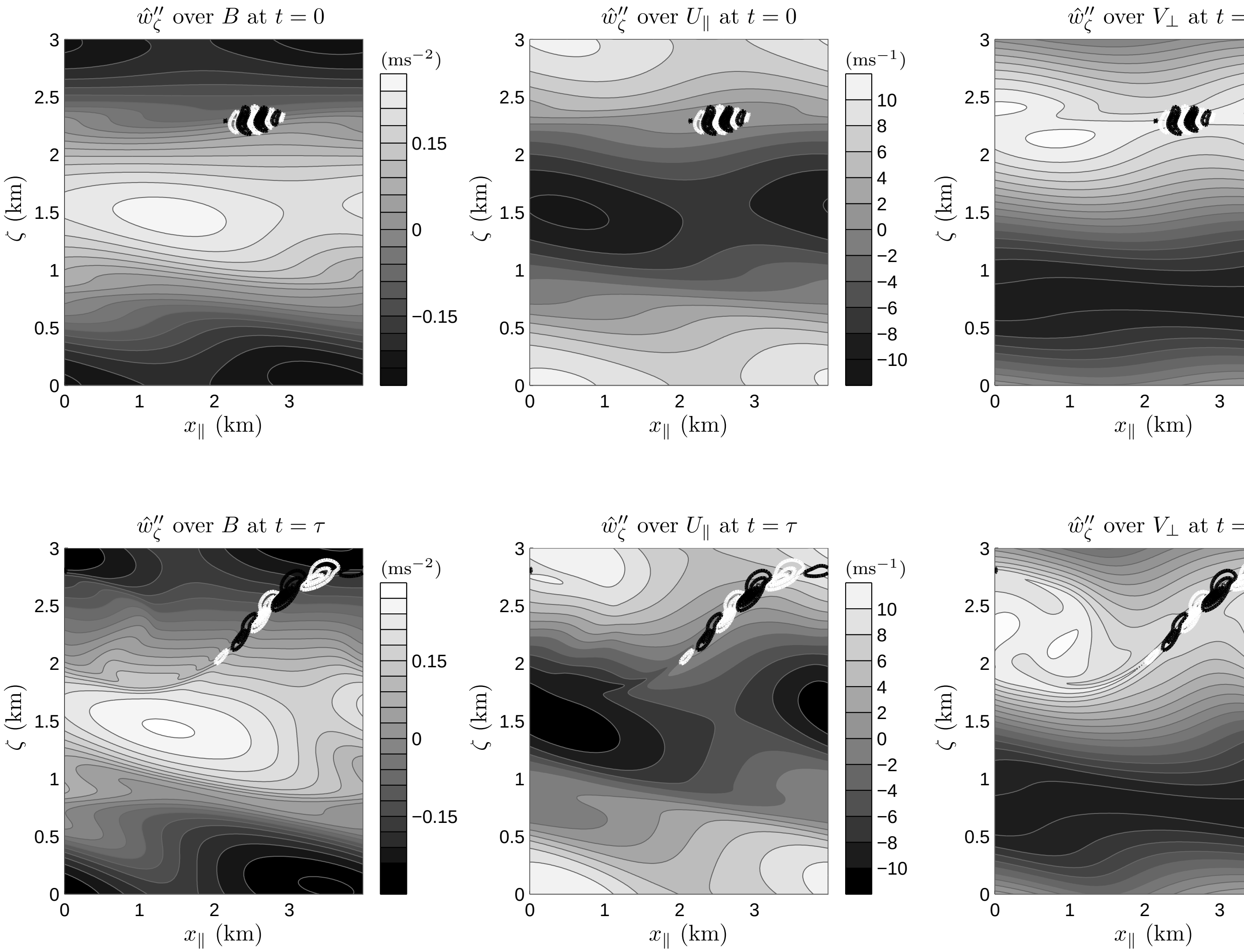

Figure 4. Contours of the real part of perturbation vertical velocity amplitude $\hat{w}''_\zeta$ at initial (*top row*) and at optimization (*bottom row*) times for 5 minute secondary singular vector superimposed on the basic state buoyancy B *(left)* and horizontal velocity fields $U_\parallel$ (*centre*) and $V_\perp$ (*right*) (shading) for statically unstable IGW perturbed by leading transverse normal mode.

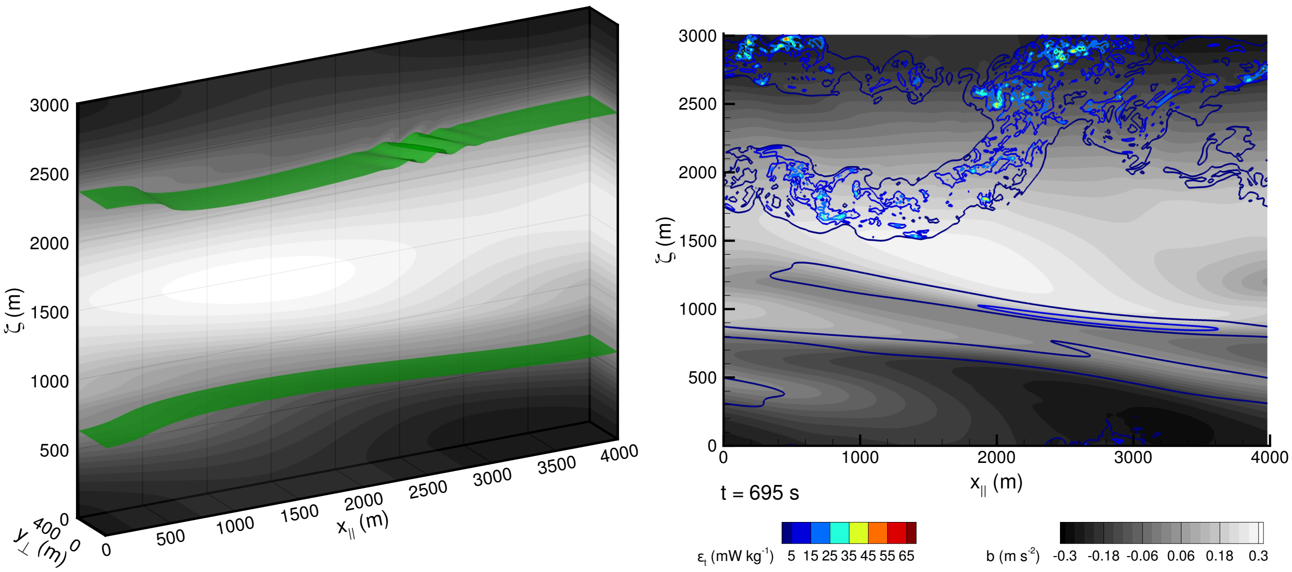

Figure 5. Snapshots of the buoyancy field from fine 3-D DNS ($1350 \times 128 \times 1000$ cells) of the statically unstable IGW: *Left*: 3-D initial condition with an isosurface at $b = -0.02\,\mathrm{m\,s^{-2}}$ (green colour). *Right*: flow field averaged in the $y_\perp$-direction at $t = 11.6\,\mathrm{min}$ (greyscale contours: buoyancy, coloured lines: total energy dissipation).

Figure 6. Comparison of wave amplitude decay (*left*) and total energy dissipation (*right*) in 2.5-D and 3-D DNS of statically unstable IGW. Dash-dot line indicates amplitude decay due to laminar viscous decay of the unperturbed wave.

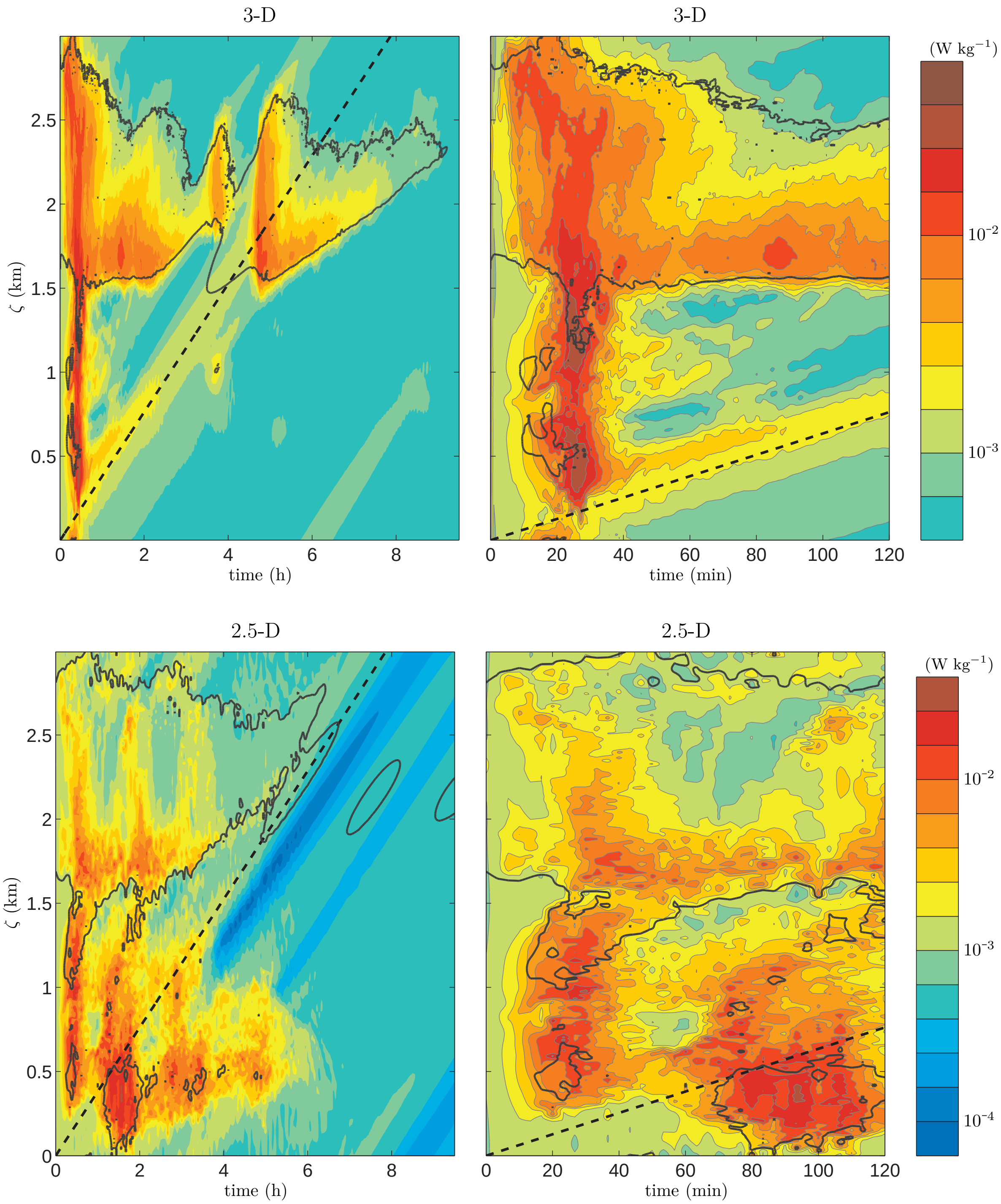

Figure 7. Spanwise and streamwise averaged total energy dissipation from 3-D (*top row*) and 2.5-D (*bottom row*) DNS of unstable IGW. Contours equally spaced on a logarithmic (base 10) scale. Dashed black line represents a fixed point in the Earth frame. Right panels are close-ups of first two hours of model time. Solid dark-grey lines represent contours of $Ri = 1/4$ (see Eq. 17).

Figure 8. Spanwise and streamwise averaged energy spectra from times of peak energy dissipation in the 2.5-D and coarse resolution ($640 \times 64 \times 500$ cells) 3-D DNS of the unstable IGW. Shaded regions show the range of values of ensembles of 2.5-D simulations. Also plotted on all panels are the spectra from the initial conditions of 2.5-D and 3-D simulations.

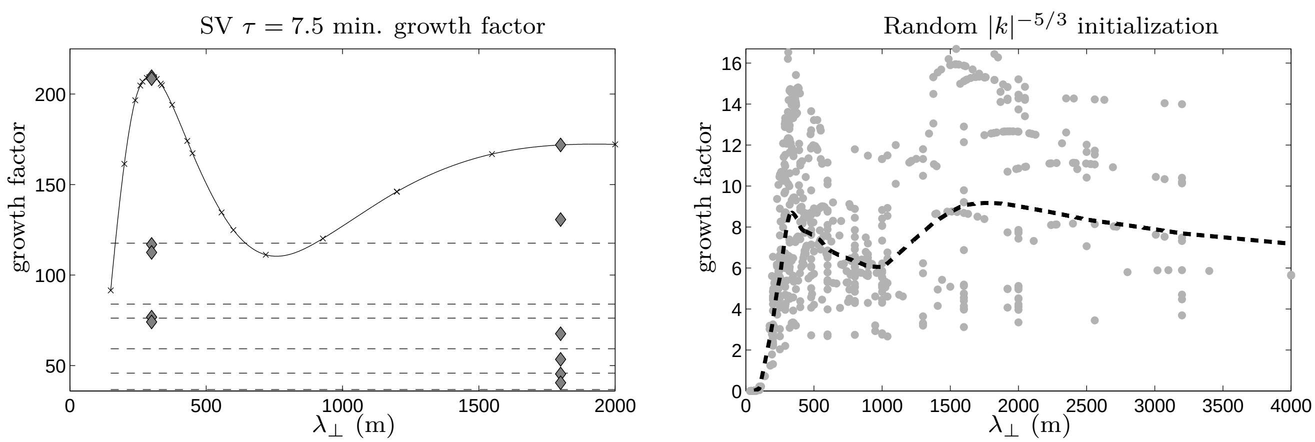

Figure 9. As in figure 3 but for optimization time 7.5 minutes and the statically stable IGW perturbed by its leading transverse singular vector. The filled diamonds mark the growth factors of the leading twelve (N.B. they come in degenerate pairs) singular vectors for $\lambda_\perp = 300$ m and $\lambda_\perp = 1800$ m.

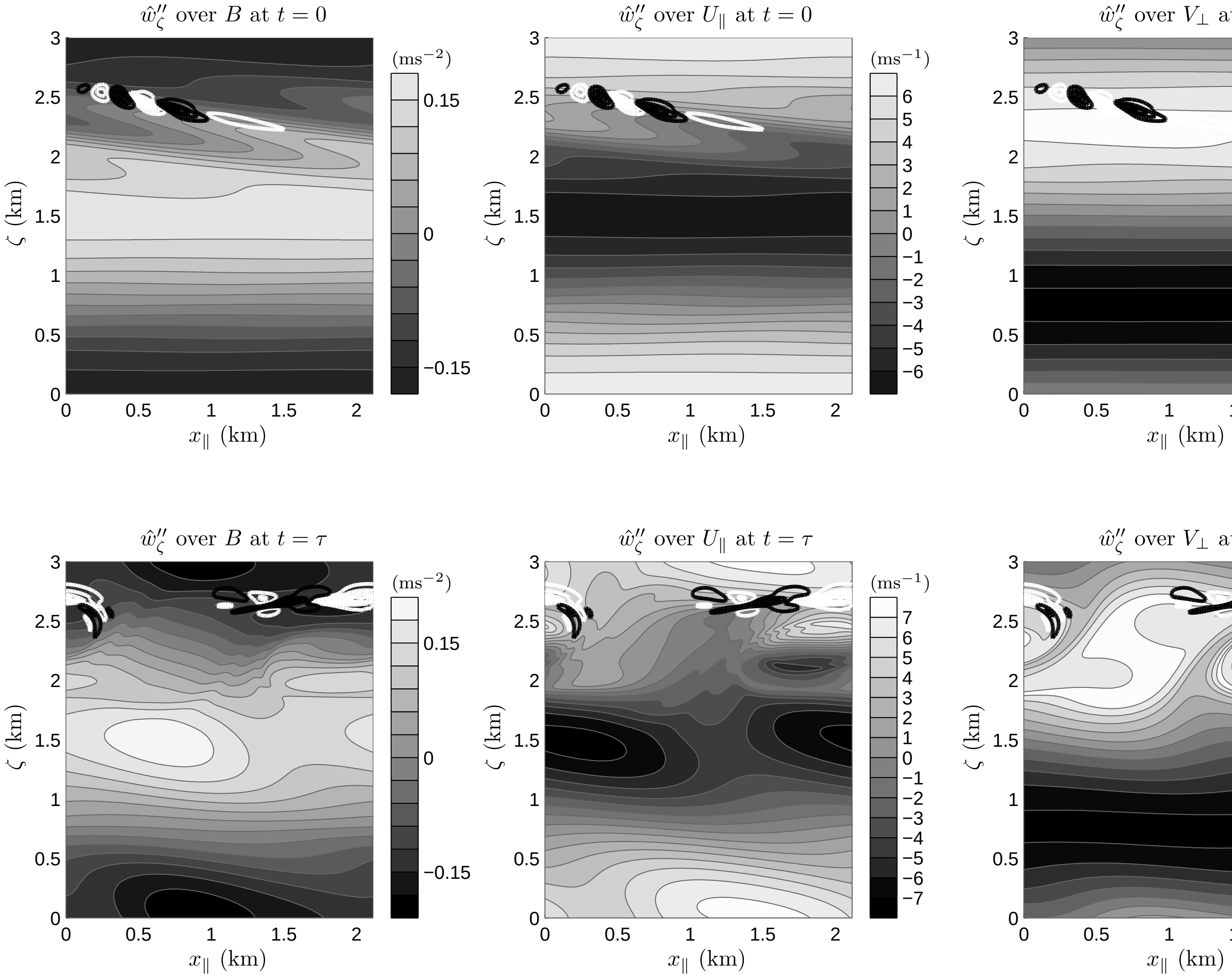

Figure 10. As in figure 4 but for optimization time $\tau = 7.5$ minutes and the statically stable IGW perturbed by its leading 7.5-minute transverse primary singular vector.

Figure 11. Snapshots of the buoyancy field from 3-D DNS ($720 \times 96 \times 1024$ cells) of the statically stable IGW: (a) 3-D initial condition with the isosurface $b = -0.03\,\mathrm{m\,s^{-2}}$ (green colour). (b) - (f) flow field averaged in the $y_\perp$-direction (greyscale contours: buoyancy, coloured lines: total energy dissipation)

Figure 12. As in figure 6 but for the statically stable IGW. The resolutions used for the 3-D DNS were $720 \times 96 \times 1024$ (fine) and $512 \times 64 \times 768$ (coarse). The curves in the lower part of the left panel show the maximum (solid line) and mean (dashed line) energy in the linear 2.5-D integration initialized with the primary SV, and the vertical dotted line marks the optimization time (7.5 minutes). For reference, the energy density in the unperturbed IGW is 54.5 $\mathrm{m^2 s^{-2}}$.

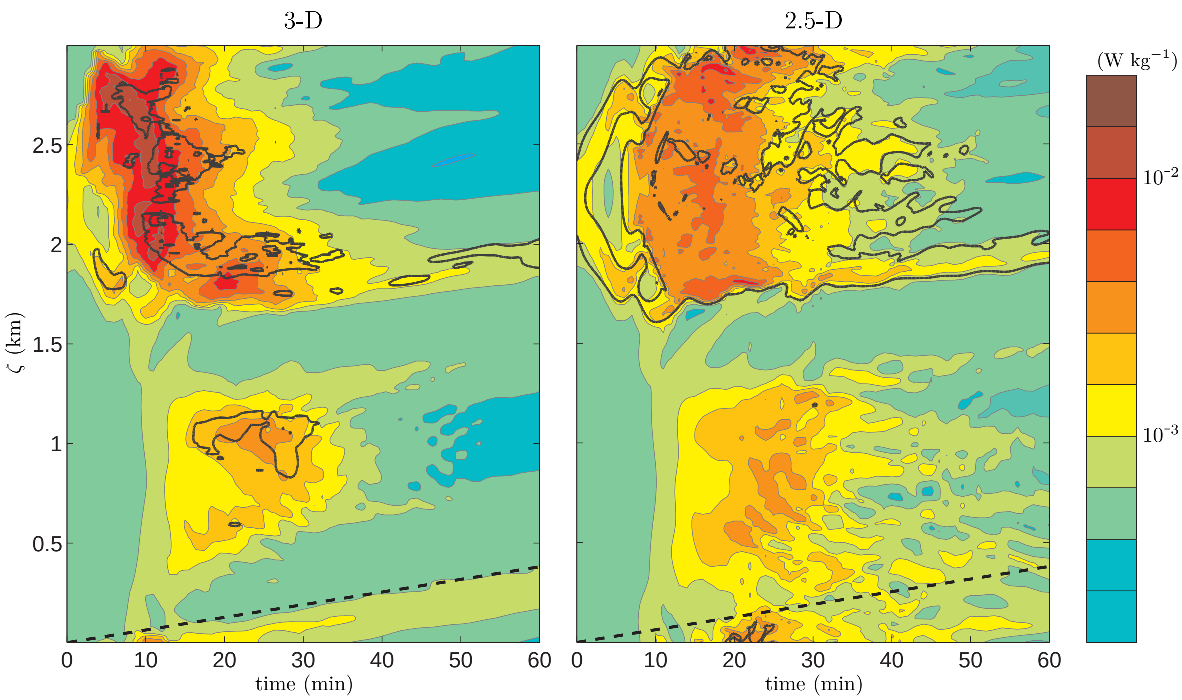

Figure 13. Spanwise and streamwise averaged total energy dissipation from the fully resolved 3-D (*left*) and 2.5-D (*right*) DNS of the statically stable IGW. Contours equally spaced on a logarithmic (base 10) scale. Solid light grey line is the contour $Ri = 1/4$ (see Eq. 17) and the heavy dashed black line represents a fixed point in the Earth-frame.

Figure 14. Kolmogorov length in the 3-D DNS of (a) the stable IGW and (b) the unstable HGW. The threshold where the simulation is supposed to be fully resolved is indicated by a horizontal line for each simulation.

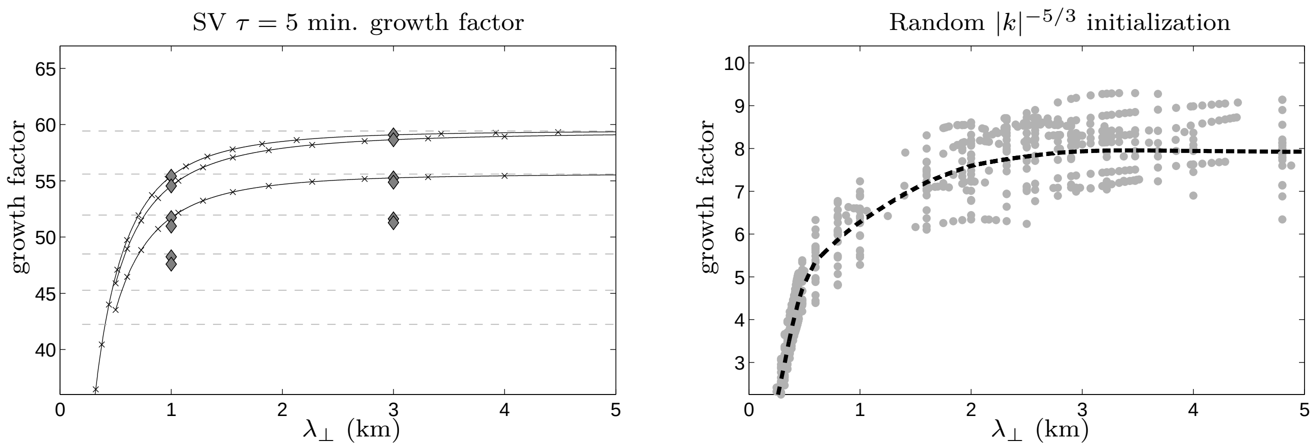

Figure 15. As in figure 3 but for the statically unstable HGW perturbed by its leading transverse singular vector. Filled diamonds in left panel indicate growth factors of leading twelve singular vectors with $\lambda_\perp = 1000$ m and $\lambda_\perp = 3000$ m.

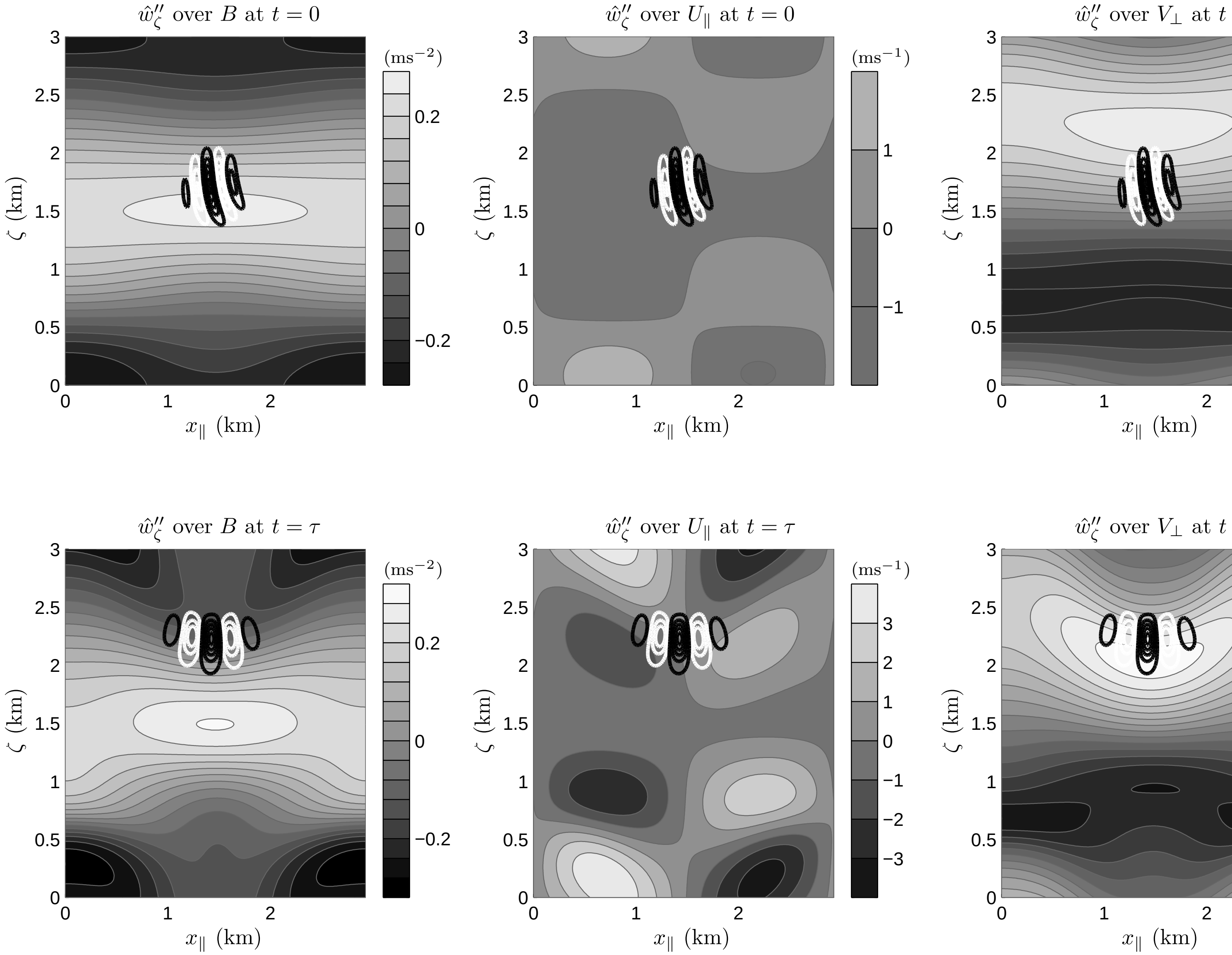

Figure 16. As in figure 4 but for the statically unstable HGW perturbed by the leading transverse normal mode.

Figure 17. Snapshots of the buoyancy field from the fine 3-D DNS (1536^3 cells) of the statically unstable HGW: (a) 3-D initial condition with the isosurface $b = 0.2\,\mathrm{m\,s^{-2}}$ (green colour). (b) - (f) flow field averaged in the $y_\perp$-direction (greyscale contours: buoyancy, coloured lines: total energy dissipation)

Figure 18. As in figure 6 but for the statically unstable HGW. The 3-D DNS were performed with 1536^3 (fine), 768^3 (coarse 1) and 384^3 (coarse 2) gridcells.

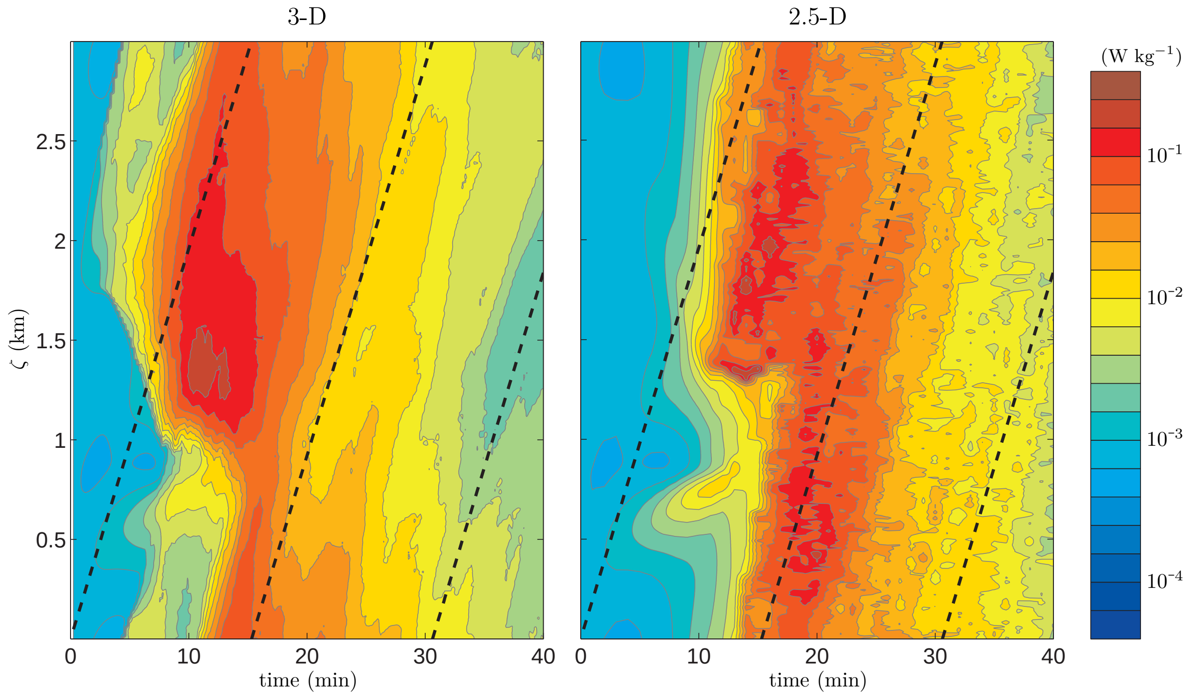

Figure 19. As in figure 13 but for the unstable HGW. The fine resolution simulation (1536^3 cells) was used for the 3-D plot.

Figure 20. As in figure 8 but for the unstable HGW. Plot times correspond to the moment of maximum energy dissipation in the 3-D simulation (15 minutes), a time after which the wave has decayed to near its saturation level (30 minutes) and the end of the simulations (90 minutes). The 3-D spectra were computed using the medium (coarse 1) resolution DNS.

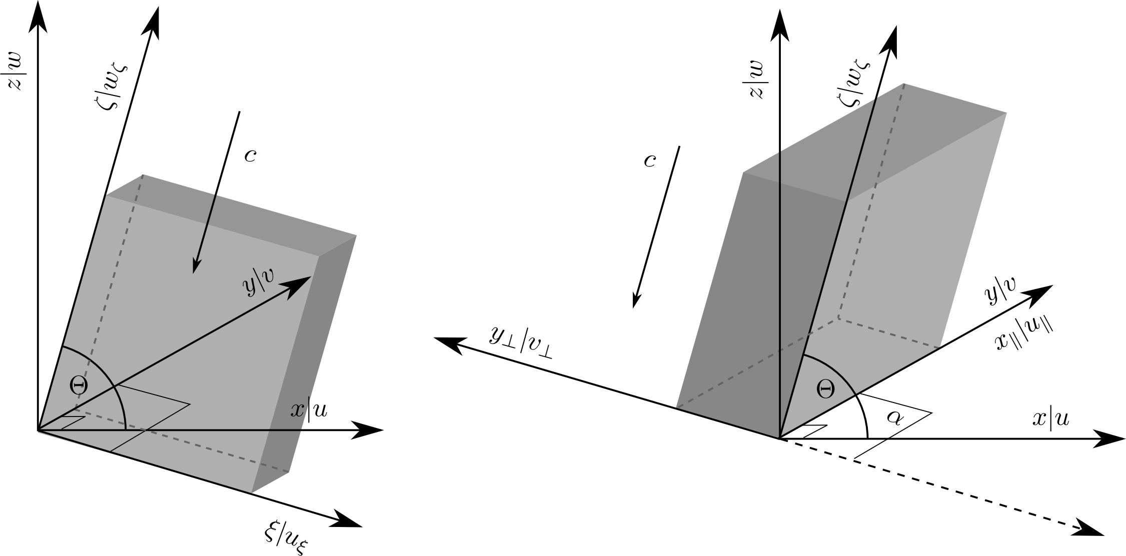

$z|w$
$\zeta|w_\zeta$
c
$y|v$
Θ
$x|u$
$\xi|u_\xi$
$z|w$
$\zeta|w_\zeta$
c
$y|v$
$x_\parallel|u_\parallel$
$y_\perp|v_\perp$
Θ
α
$x|u$

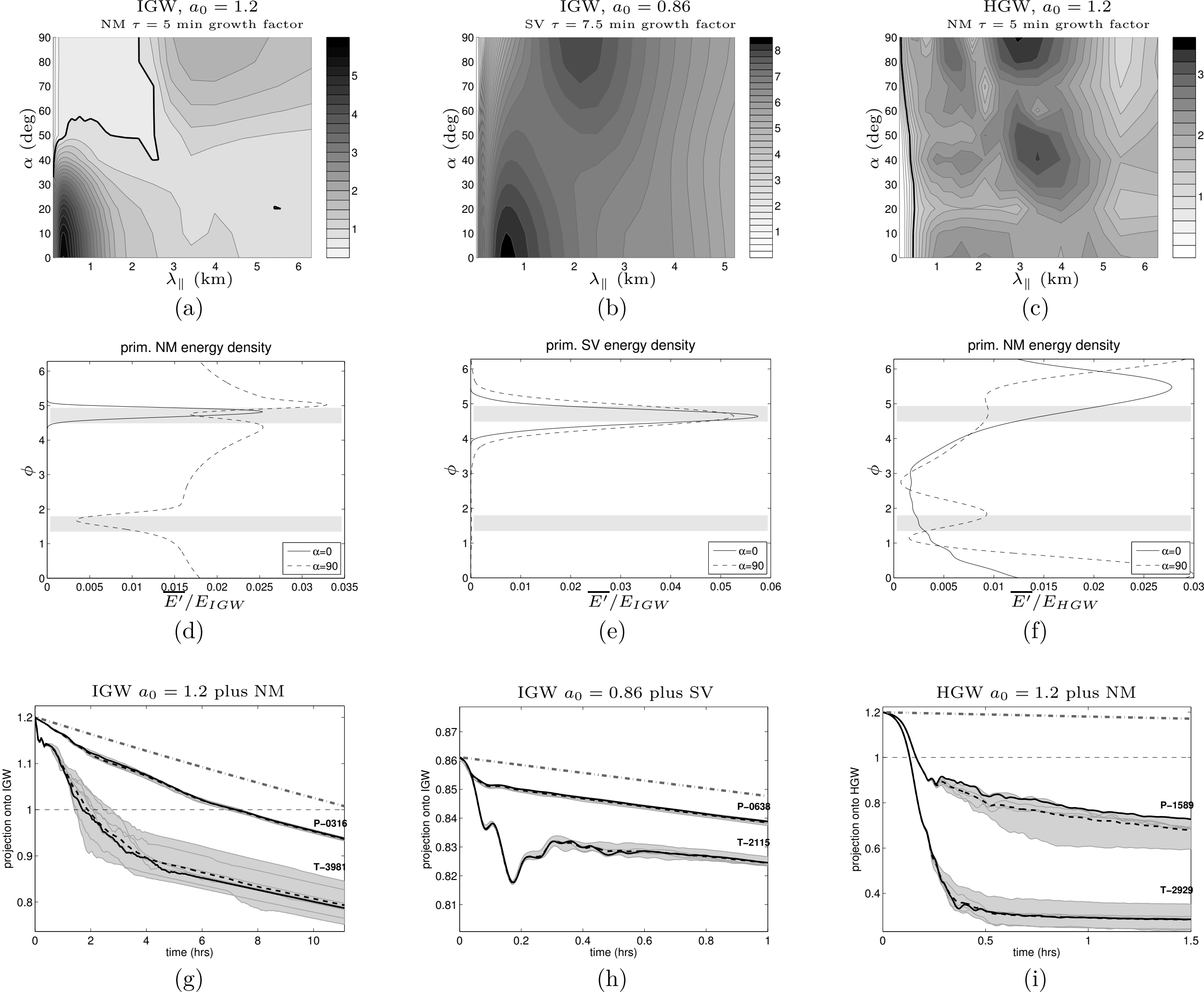

IGW, $a_0 = 1.2$
NM $\tau = 5$ min growth factor
IGW, $a_0 = 0.86$
SV $\tau = 7.5$ min growth factor
HGW, $a_0 = 1.2$
NM $\tau = 5$ min growth factor
α (deg)
$\lambda_\parallel$ (km)
(a)
(b)
(c)
prim. NM energy density
prim. SV energy density
prim. NM energy density
ϕ
α=0
α=90
$\overline{E'}/E_{IGW}$
$\overline{E'}/E_{HGW}$
(d)
(e)
(f)
IGW $a_0 = 1.2$ plus NM
IGW $a_0 = 0.86$ plus SV
HGW $a_0 = 1.2$ plus NM
projection onto IGW
projection onto HGW
time (hrs)
P–0316
T–3981
P–0638
T–2115
P–1589
T–2929
(g)
(h)
(i)

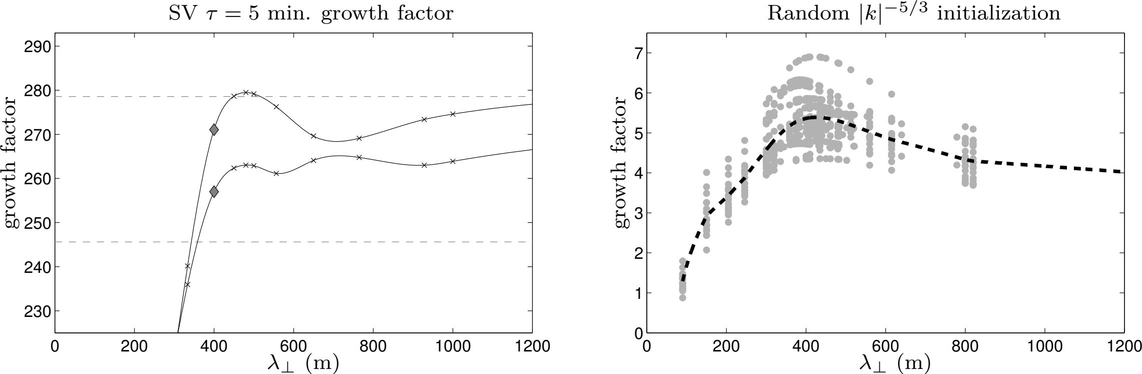

SV $\tau = 5$ min. growth factor
growth factor
$\lambda_\perp$ (m)
290
280
270
260
250
240
230
0
200
400
600
800
1000
1200
Random $|k|^{-5/3}$ initialization
growth factor
$\lambda_\perp$ (m)
7
6
5
4
3
2
1
0
0
200
400
600
800
1000
1200

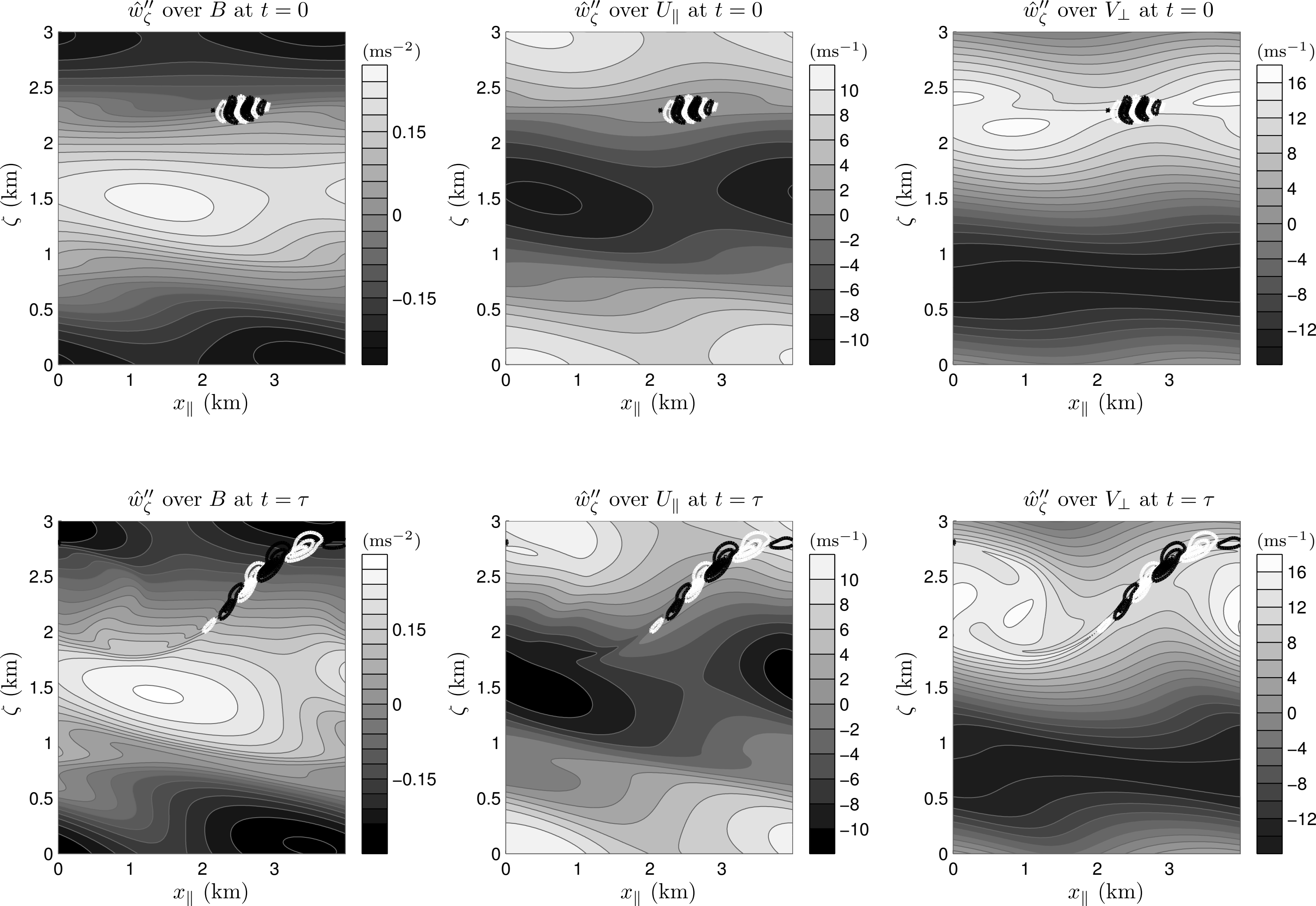

$\hat{w}''_\zeta$ over B at $t=0$
$\hat{w}''_\zeta$ over $U_\parallel$ at $t=0$
$\hat{w}''_\zeta$ over $V_\perp$ at $t=0$
$\hat{w}''_\zeta$ over B at $t=\tau$
$\hat{w}''_\zeta$ over $U_\parallel$ at $t=\tau$
$\hat{w}''_\zeta$ over $V_\perp$ at $t=\tau$
ζ (km)
$x_\parallel$ (km)
(ms^{-2})
(ms^{-1})
0.15
0
−0.15
10
8
6
4
2
−2
−4
−6
−8
−10
16
12
−12

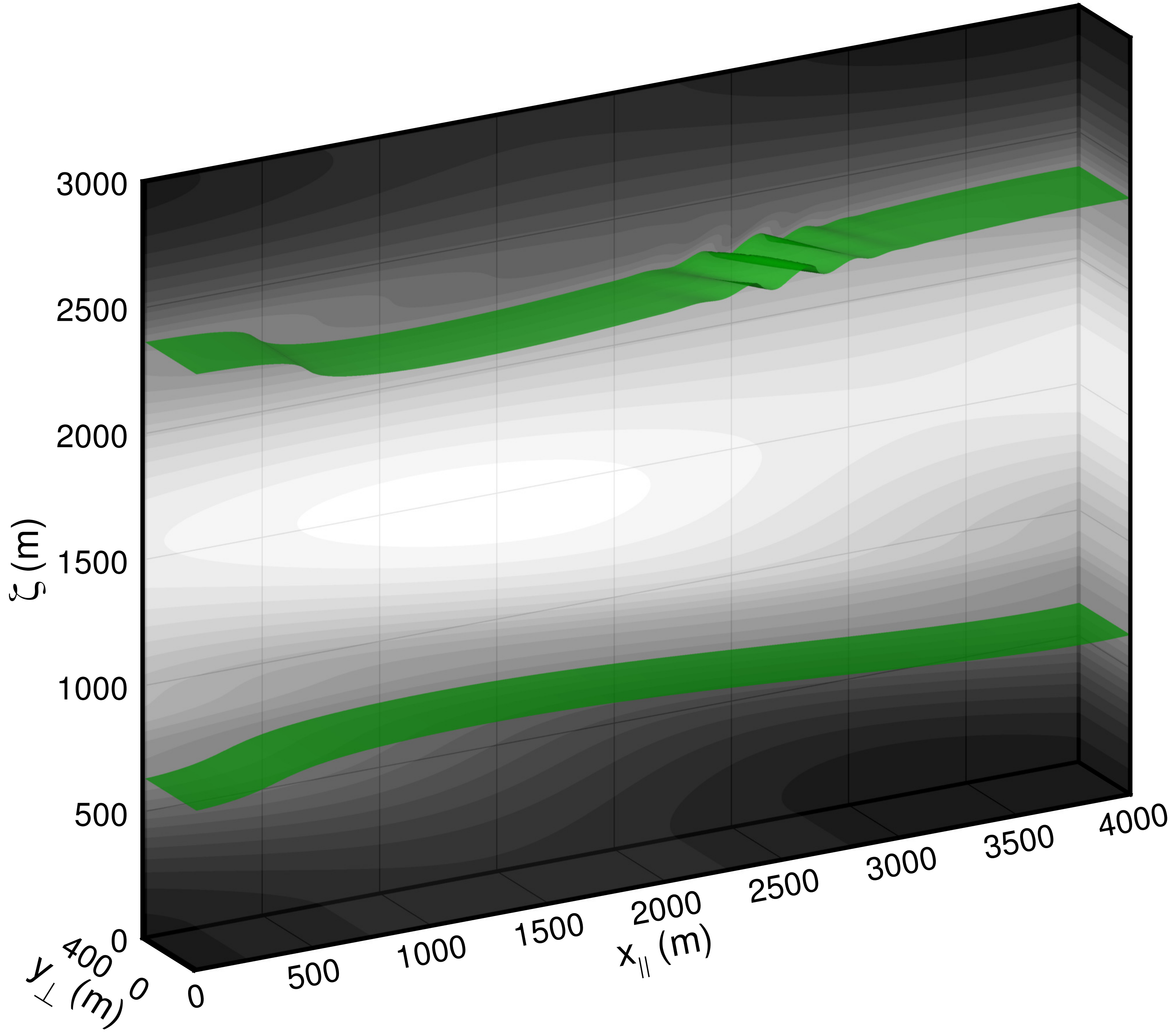

3000
2500
2000
1500
1000
500
0
ζ (m)
0
500
1000
1500
2000
2500
3000
3500
4000
x∥ (m)
400
0
y⊥ (m)

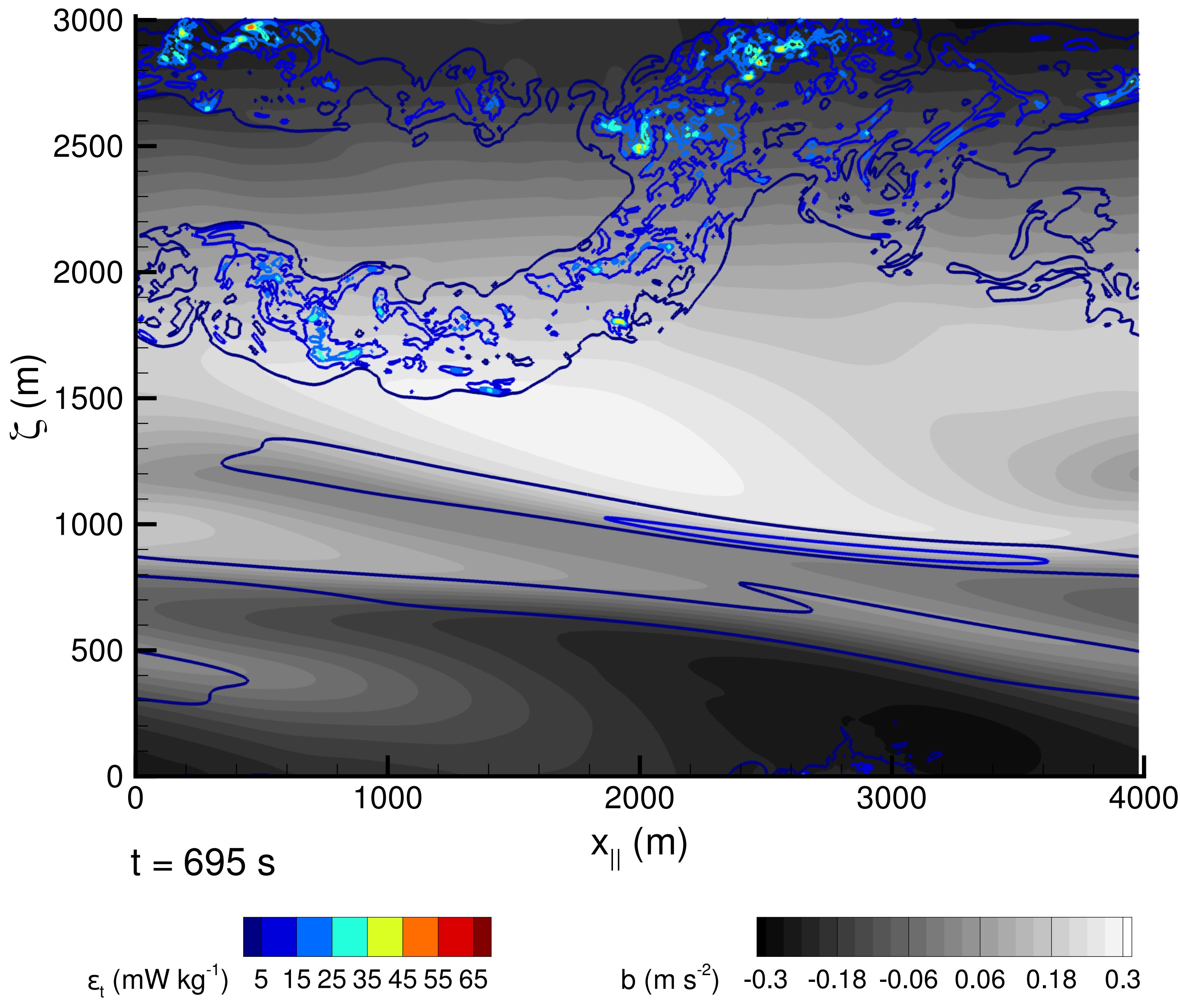

3000
2500
2000
1500
1000
500
0
ζ (m)
0
1000
2000
3000
4000
x|| (m)
t = 695 s
ε_t (mW kg^-1)
5 15 25 35 45 55 65
b (m s^-2)
-0.3 -0.18 -0.06 0.06 0.18 0.3

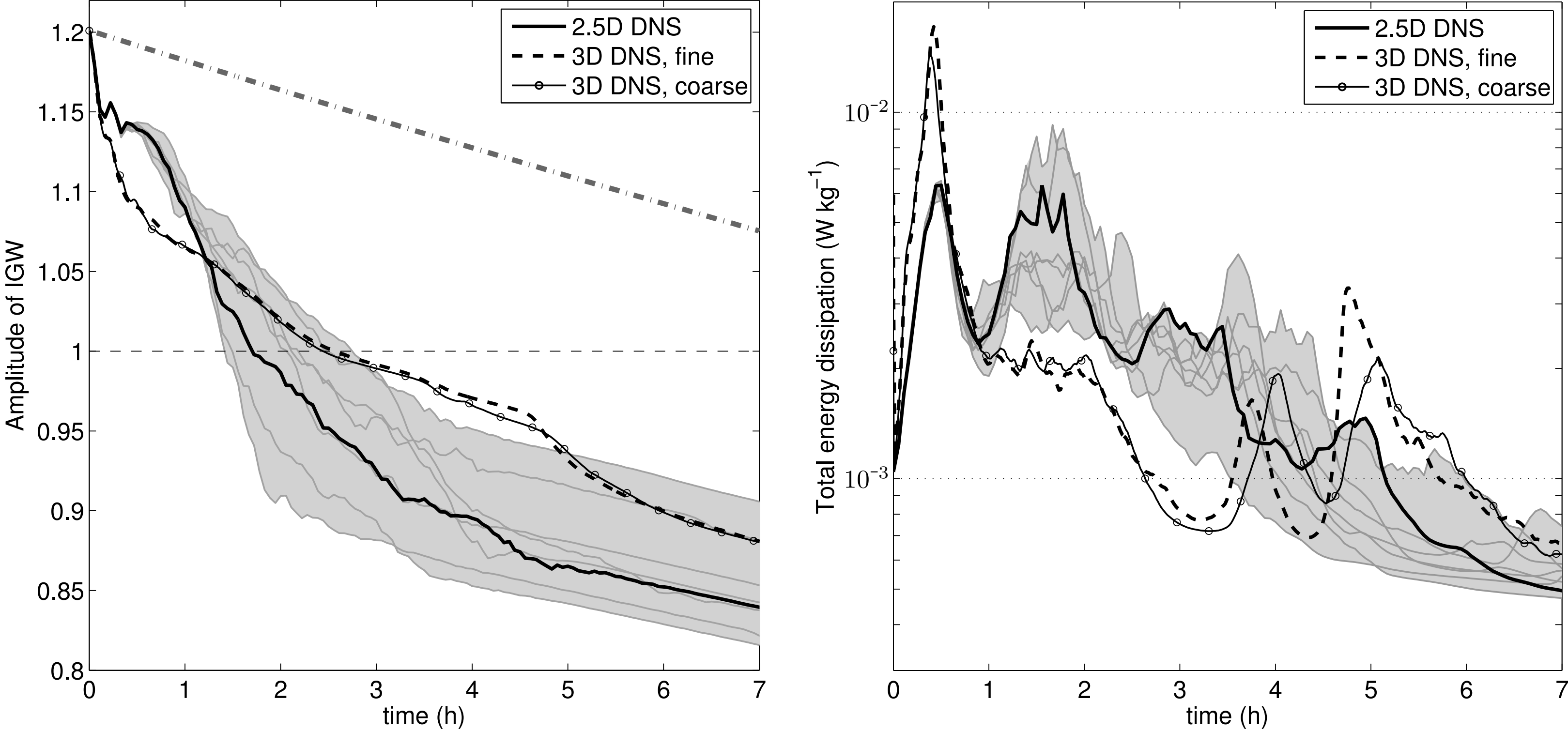

2.5D DNS
3D DNS, fine
3D DNS, coarse
Amplitude of IGW
time (h)
1.2
1.15
1.1
1.05
1
0.95
0.9
0.85
0.8
0
1
2
3
4
5
6
7
Total energy dissipation (W kg^{-1})
10^{-2}
10^{-3}

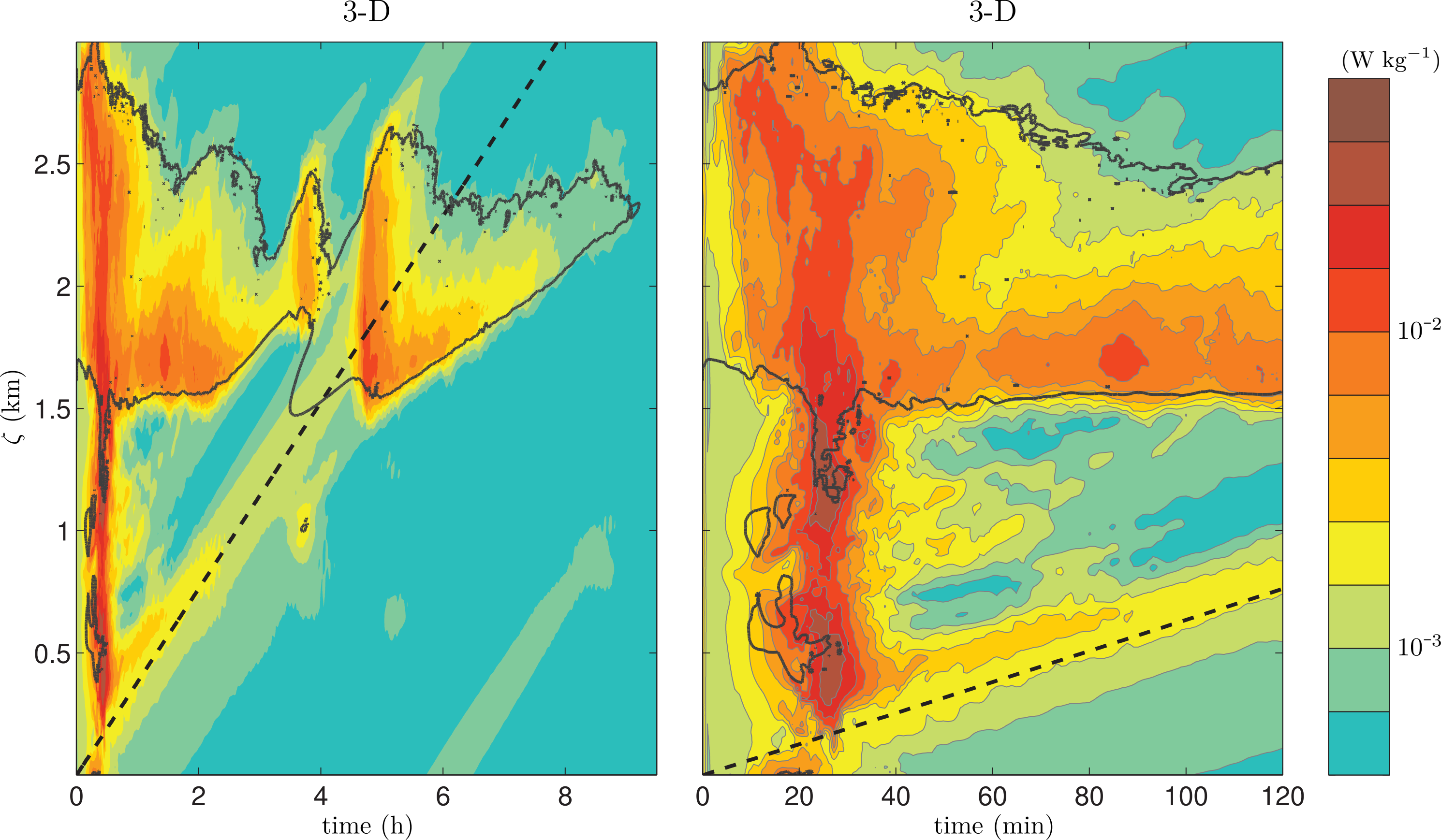

3-D
3-D
(W kg^{-1})
10^{-2}
10^{-3}
ζ (km)
2.5
2
1.5
1
0.5
0
2
4
6
8
time (h)
0
20
40
60
80
100
120
time (min)

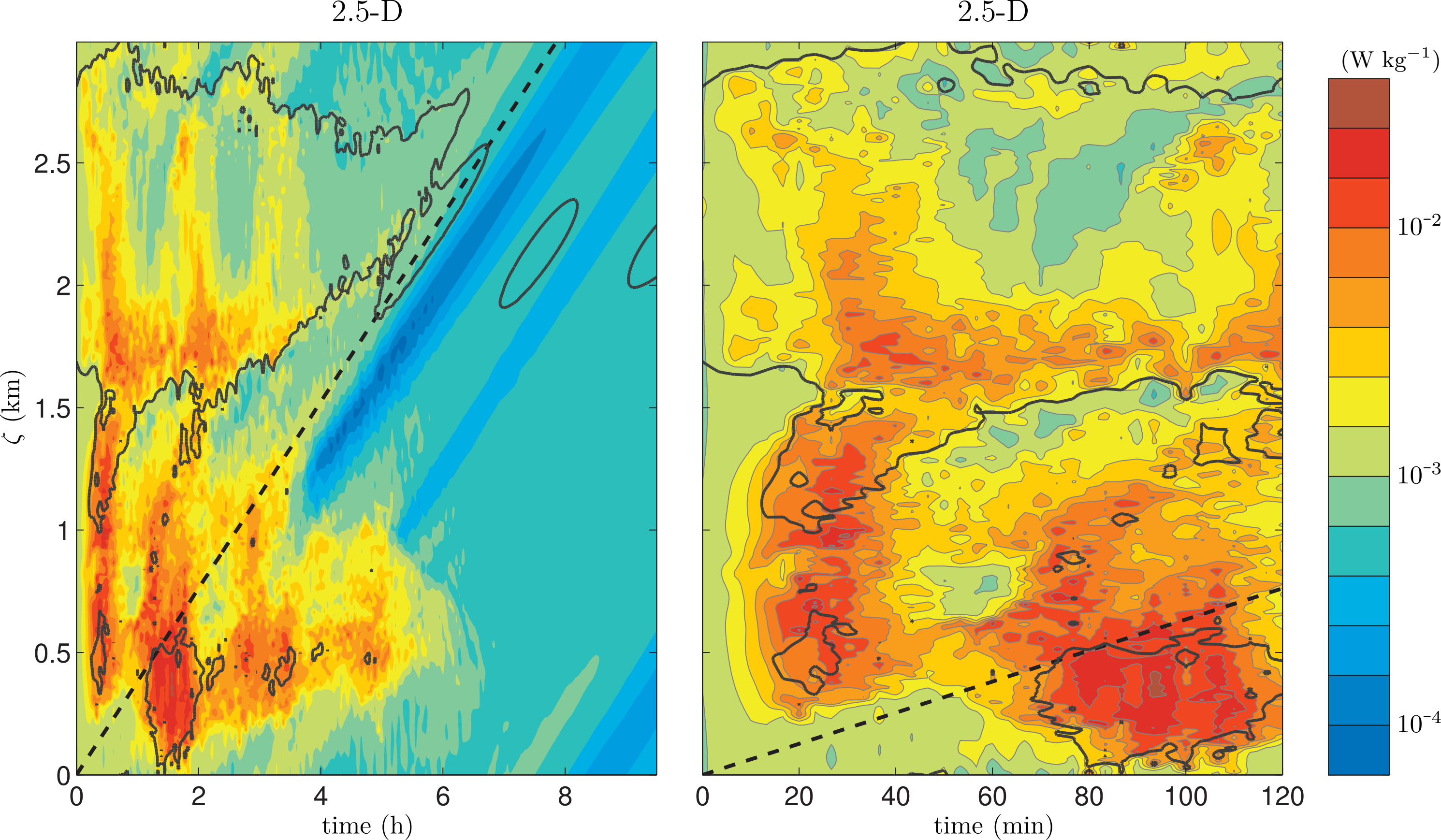
2.5-D
2.5-D
(W kg^{-1})
10^{-2}
10^{-3}
10^{-4}
ζ (km)
0
0.5
1
1.5
2
2.5
time (h)
0
2
4
6
8
time (min)
0
20
40
60
80
100
120

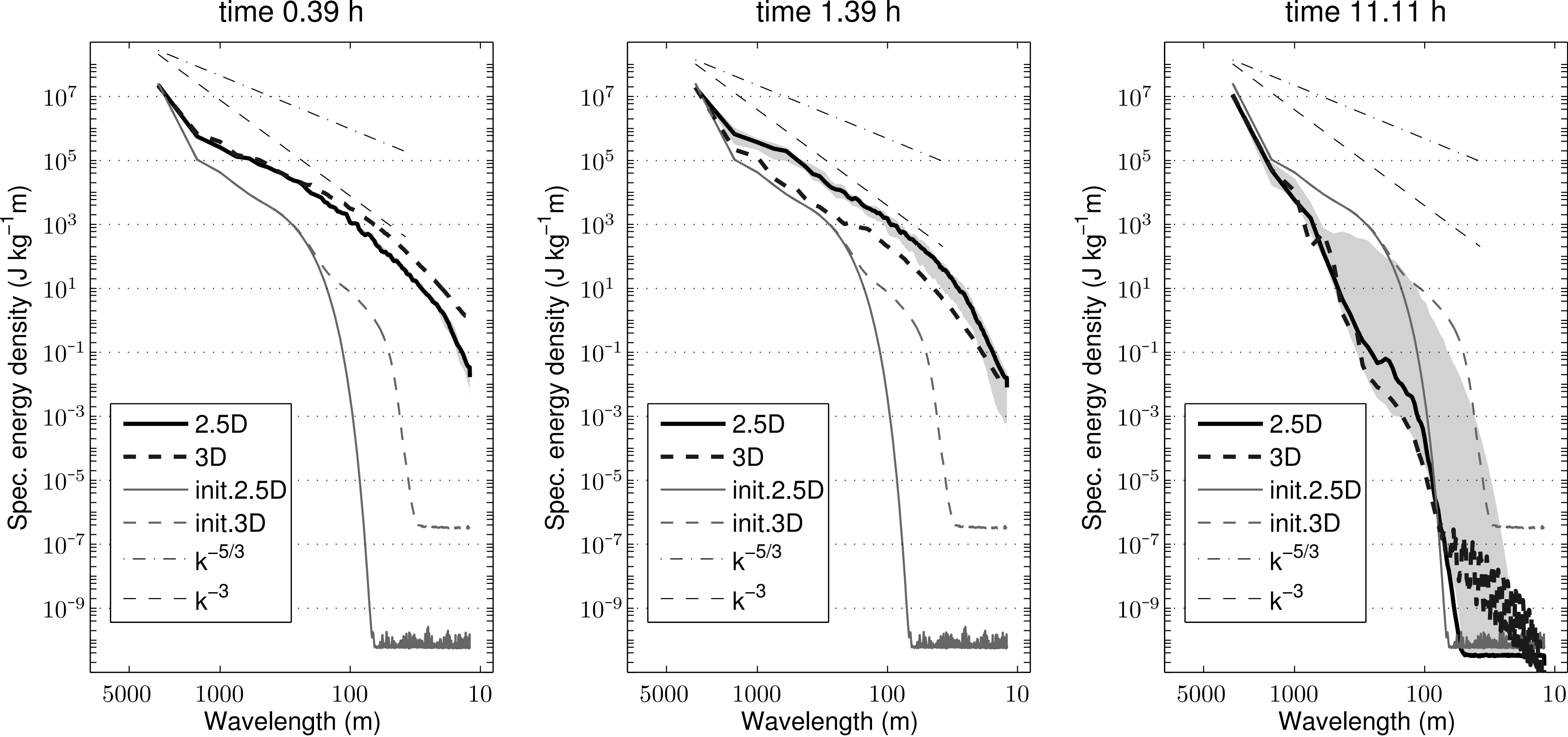

time 0.39 h
time 1.39 h
time 11.11 h
Spec. energy density (J kg^{-1} m)
Wavelength (m)
10^{7}
10^{5}
10^{3}
10^{1}
10^{-1}
10^{-3}
10^{-5}
10^{-7}
10^{-9}
5000
1000
100
10
2.5D
3D
init.2.5D
init.3D
$k^{-5/3}$
k^{-3}

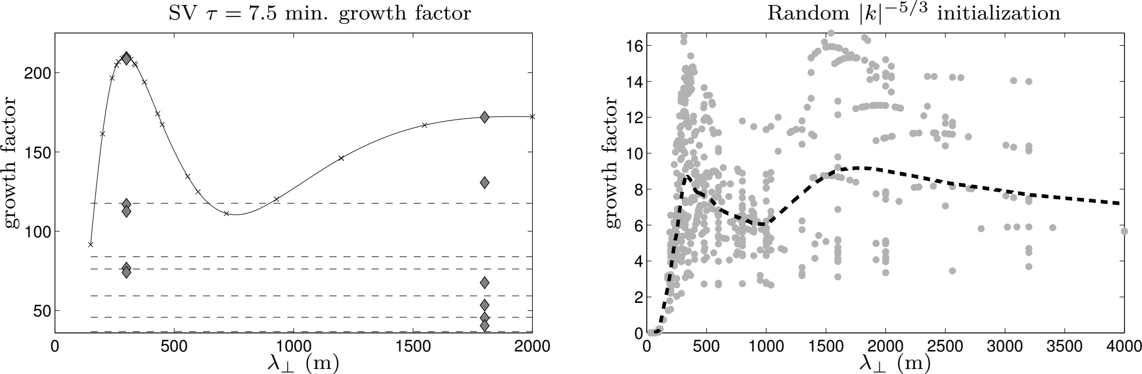

SV $\tau = 7.5$ min. growth factor
growth factor
$\lambda_\perp$ (m)
0
500
1000
1500
2000
50
100
150
200
Random $|k|^{-5/3}$ initialization
growth factor
$\lambda_\perp$ (m)
0
500
1000
1500
2000
2500
3000
3500
4000
0
2
4
6
8
10
12
14
16

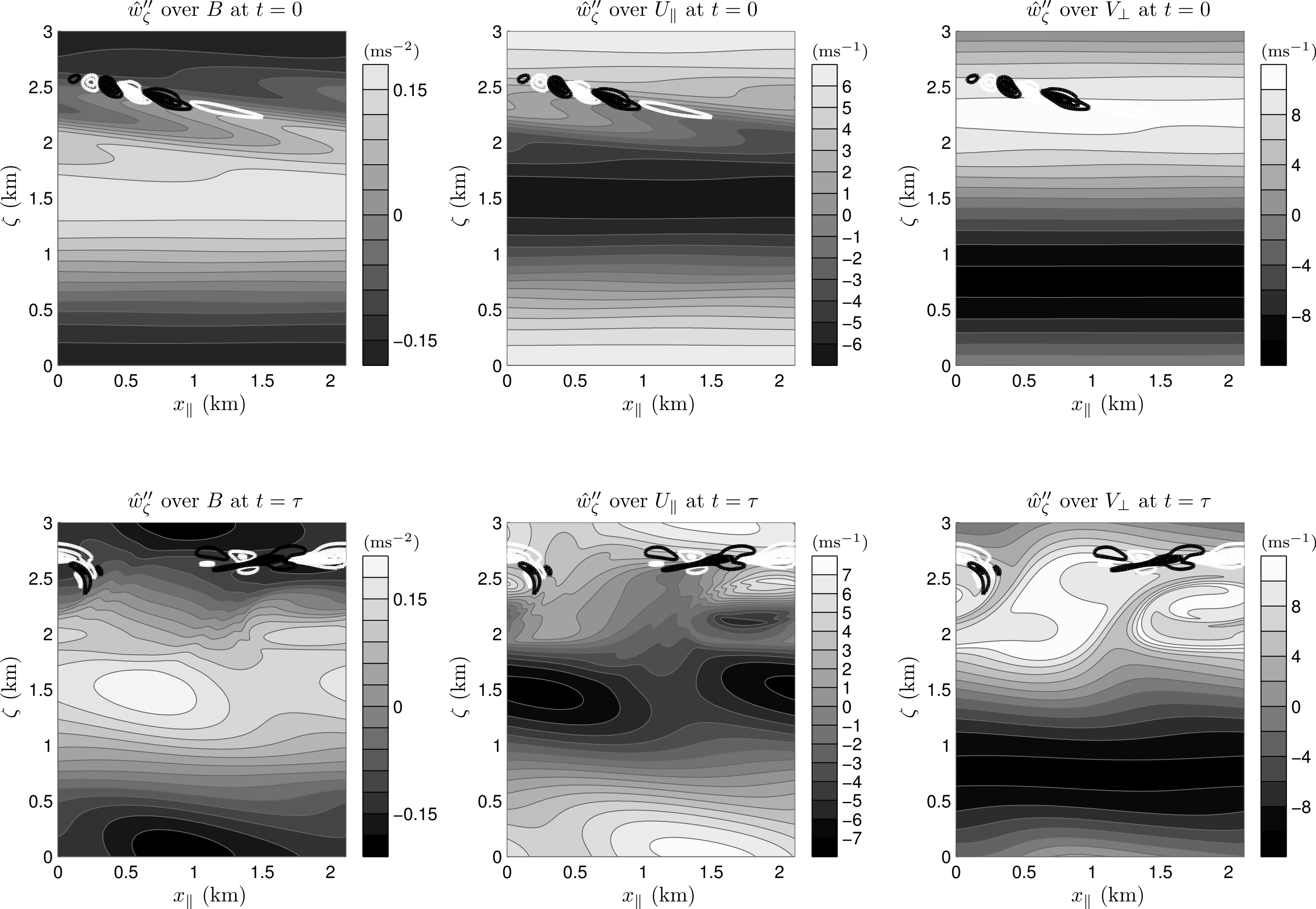
$\hat{w}''_\zeta$ over B at $t=0$
$\hat{w}''_\zeta$ over $U_\parallel$ at $t=0$
$\hat{w}''_\zeta$ over $V_\perp$ at $t=0$
$\hat{w}''_\zeta$ over B at $t=\tau$
$\hat{w}''_\zeta$ over $U_\parallel$ at $t=\tau$
$\hat{w}''_\zeta$ over $V_\perp$ at $t=\tau$
ζ (km)
$x_\parallel$ (km)
(ms^{-2})
(ms^{-1})
0.15
0
−0.15
7
6
5
4
3
2
1
0
−1
−2
−3
−4
−5
−6
−7
8
4
0
−4
−8

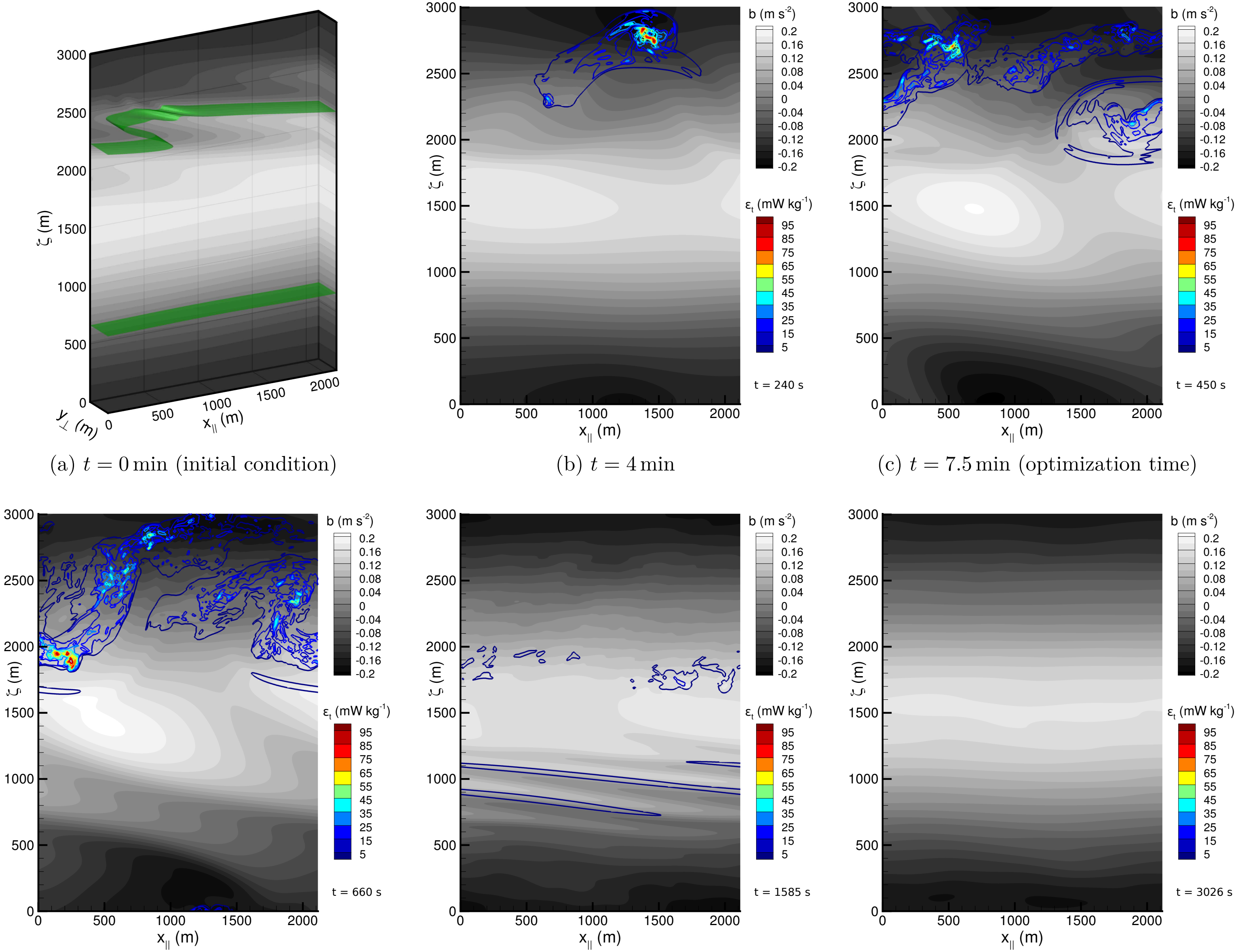

(a) $t = 0\,\text{min}$ (initial condition)

(b) $t = 4\,\text{min}$

(c) $t = 7.5\,\text{min}$ (optimization time)

(d) $t = 11\,\text{min}$ (max. dissipation)

(e) $t = 26\,\text{min}$

(f) $t = 50\,\text{min}$

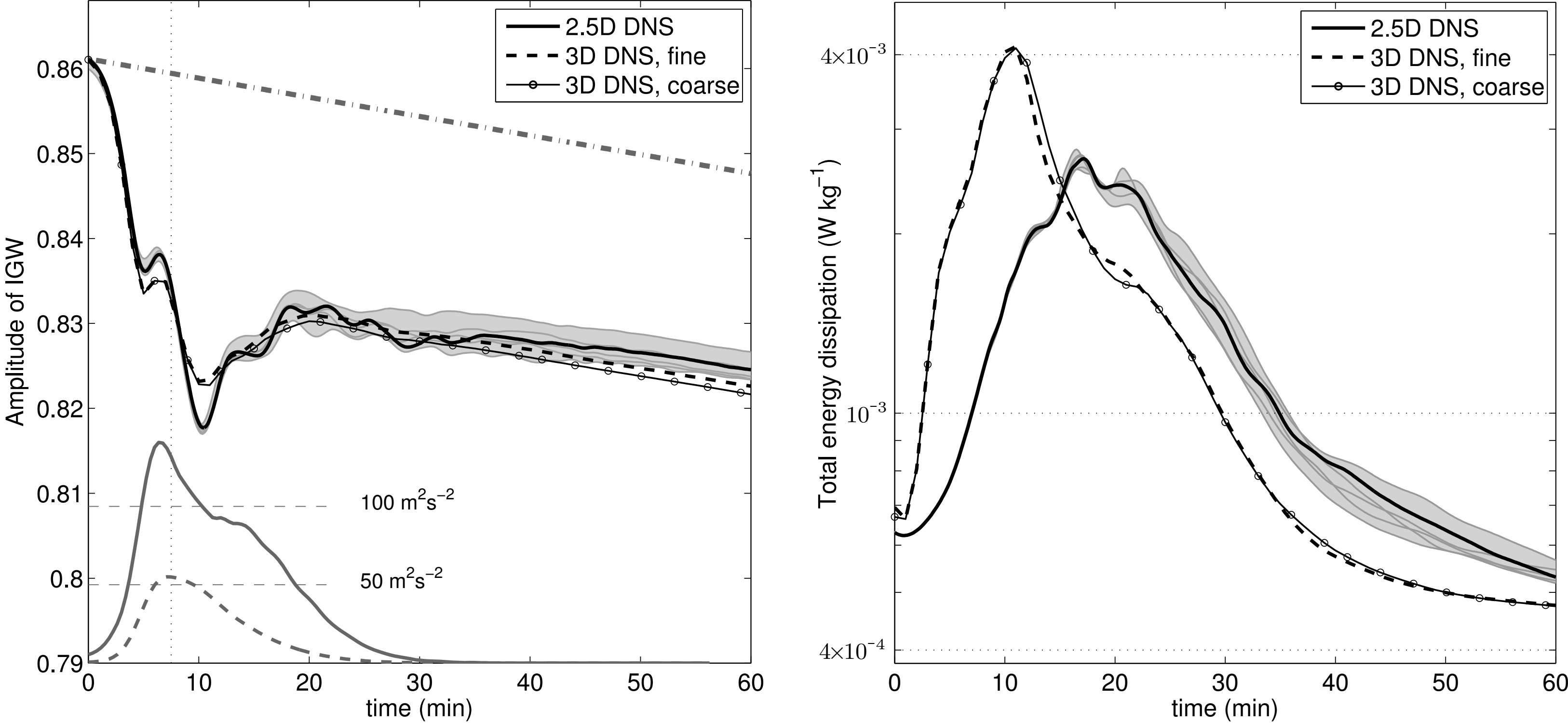

2.5D DNS
3D DNS, fine
3D DNS, coarse
Amplitude of IGW
0.86
0.85
0.84
0.83
0.82
0.81
0.8
0.79
100 m^{2}s^{-2}
50 m^{2}s^{-2}
0
10
20
30
40
50
60
time (min)
Total energy dissipation (W kg^{-1})
4×10^{-3}
10^{-3}
4×10^{-4}

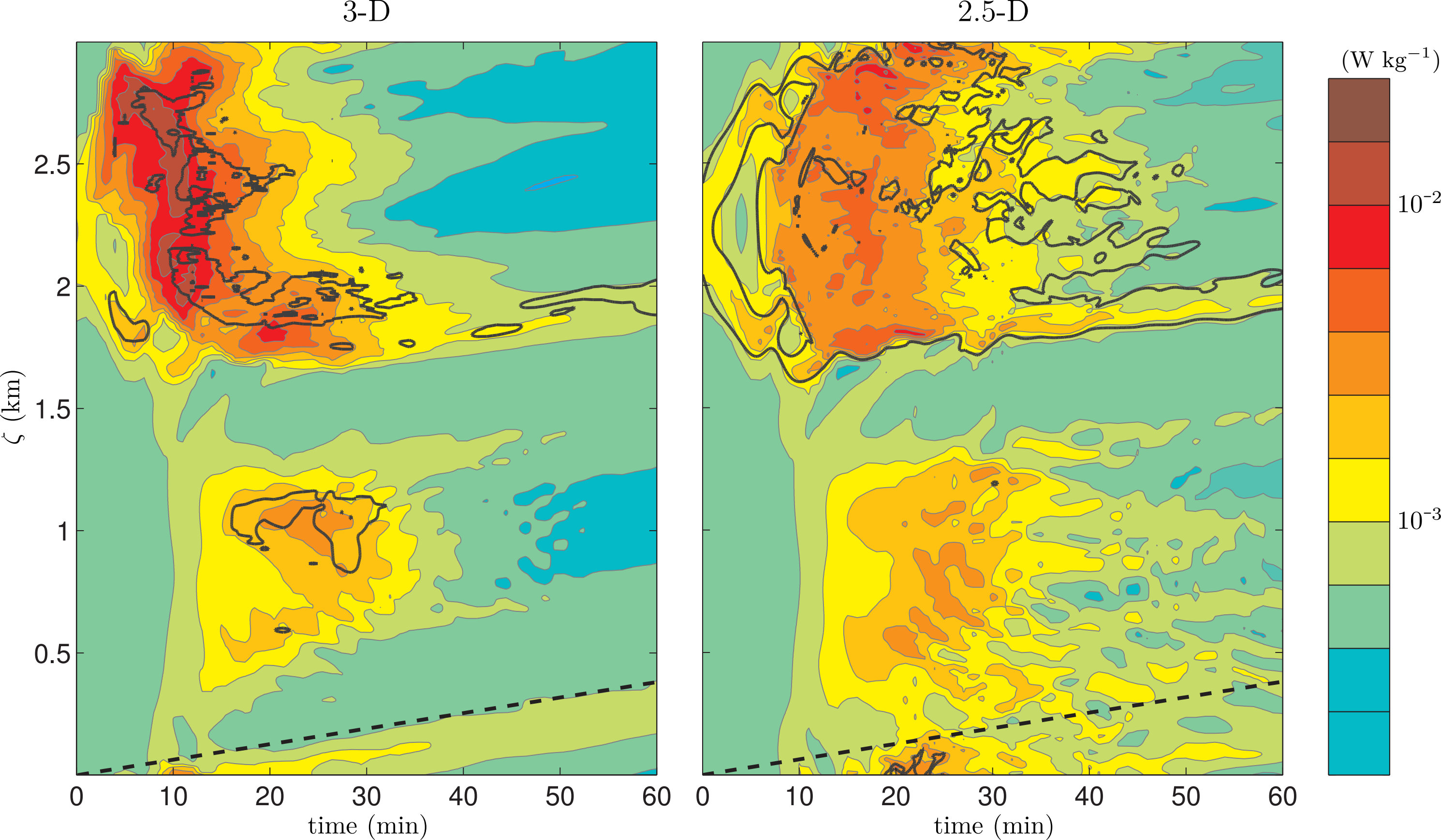

3-D
2.5-D
ζ (km)
2.5
2
1.5
1
0.5
0
10
20
30
40
50
60
time (min)
(W kg⁻¹)
10⁻²
10⁻³

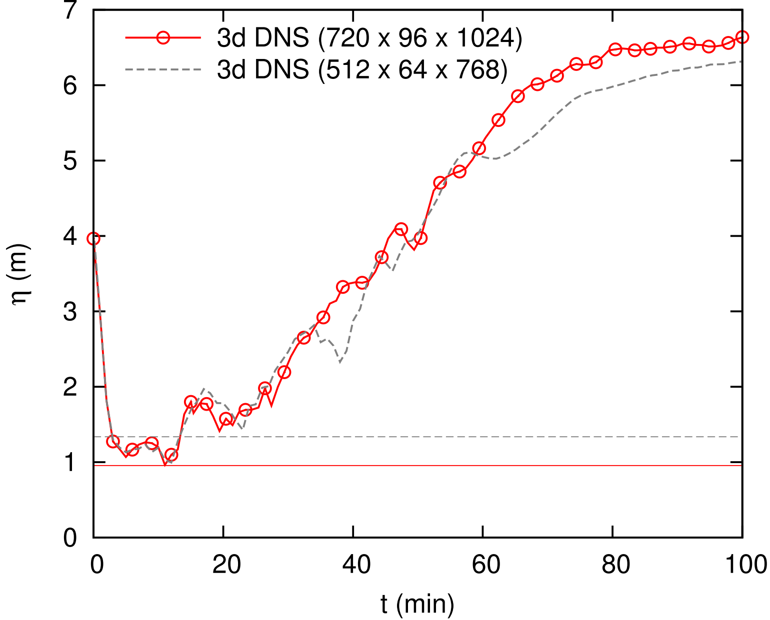

(a) stable IGW (case II)

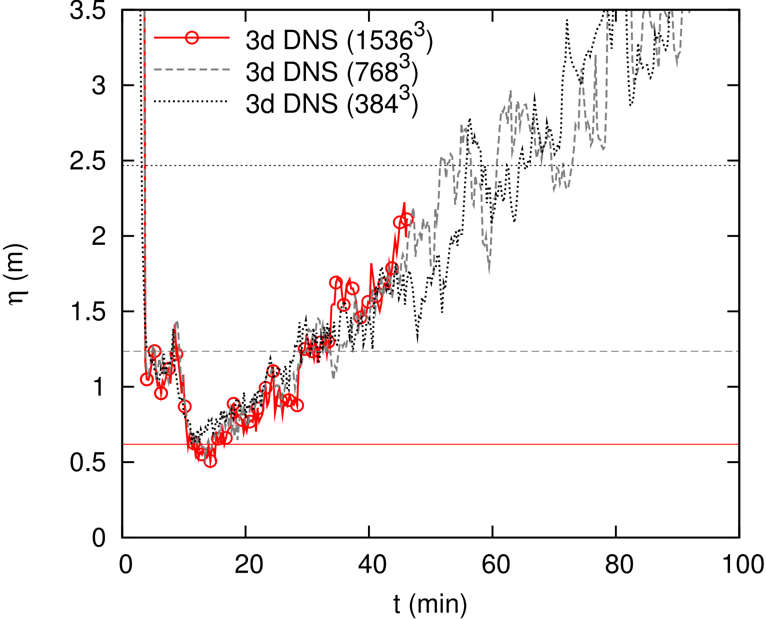

(b) unstable HGW (case III)

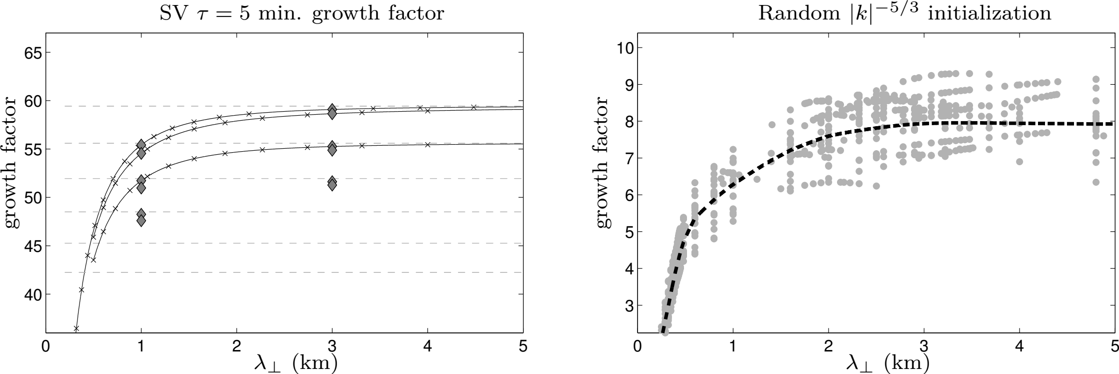

SV $\tau = 5$ min. growth factor
growth factor
$\lambda_\perp$ (km)
Random $|k|^{-5/3}$ initialization
growth factor
$\lambda_\perp$ (km)

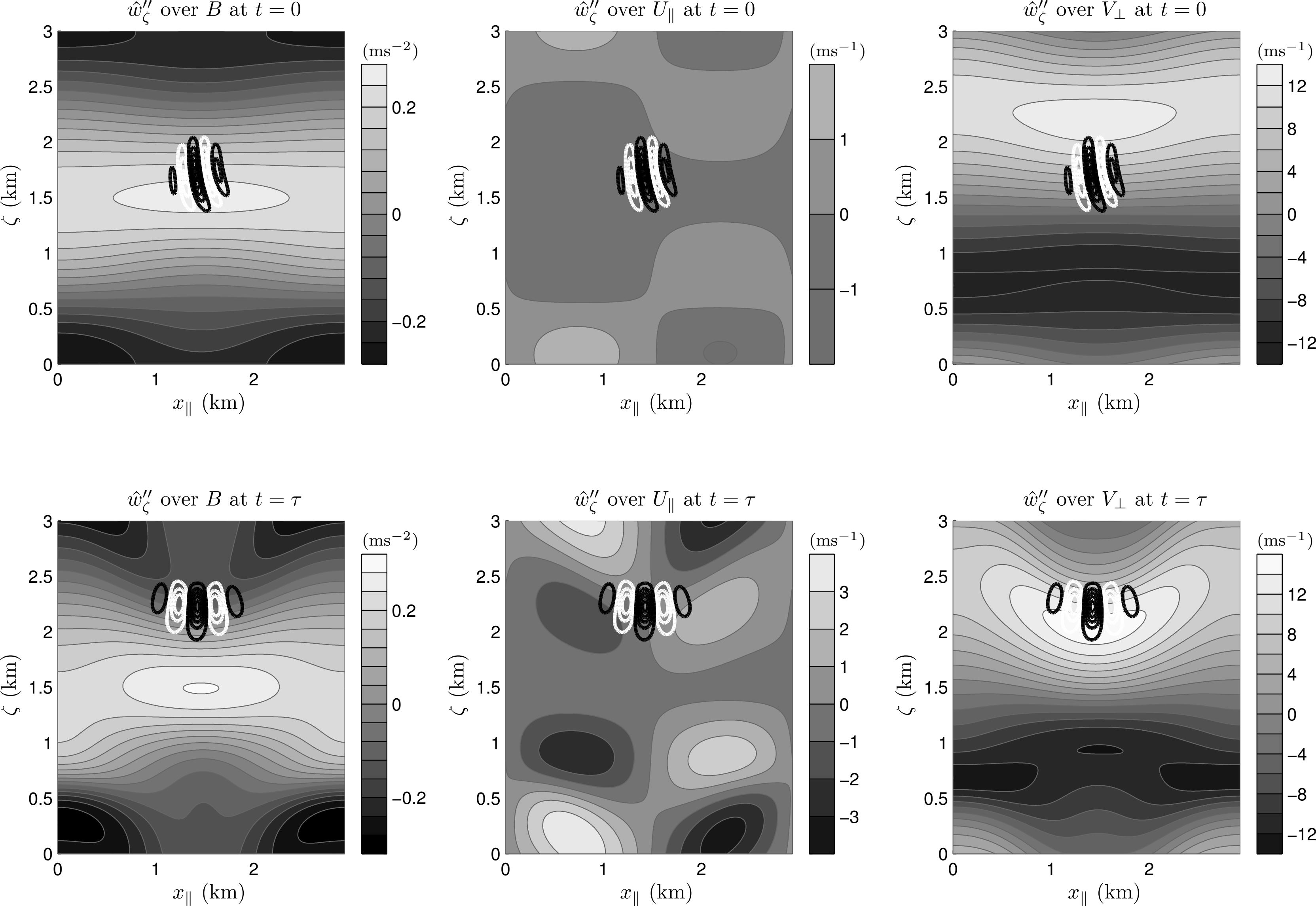
$\hat{w}''_\zeta$ over B at $t = 0$
$\hat{w}''_\zeta$ over $U_\parallel$ at $t = 0$
$\hat{w}''_\zeta$ over $V_\perp$ at $t = 0$
$\hat{w}''_\zeta$ over B at $t = \tau$
$\hat{w}''_\zeta$ over $U_\parallel$ at $t = \tau$
$\hat{w}''_\zeta$ over $V_\perp$ at $t = \tau$
ζ (km)
$x_\parallel$ (km)
(ms^{-2})
(ms^{-1})

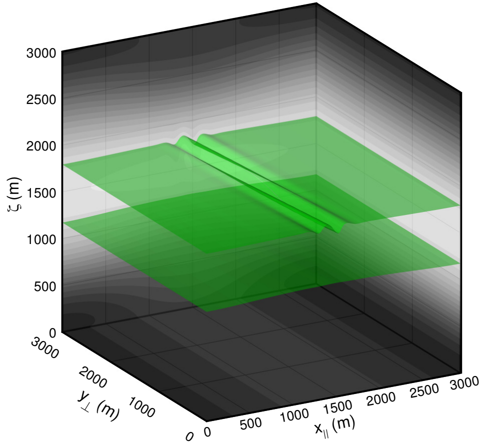

(a) $t = 0\,\text{min}$ (initial condition)

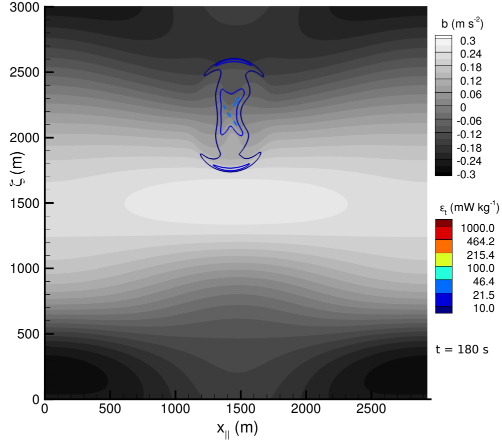

(b) $t = 3\,\text{min}$

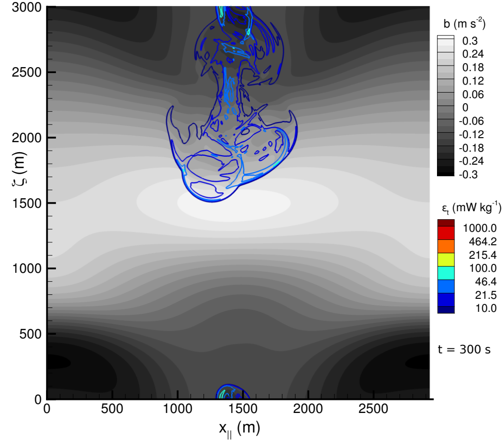

(c) $t = 5\,\text{min}$ (optimization time)

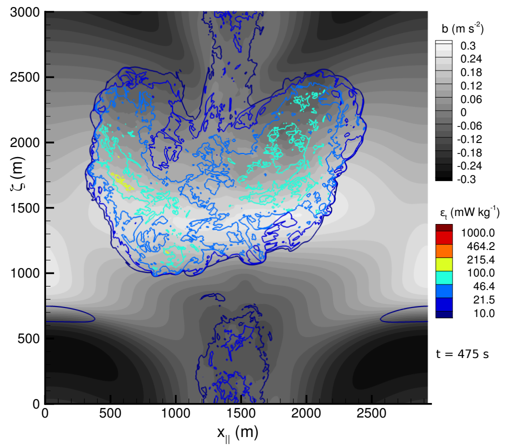

(d) $t = 8\,\text{min}$

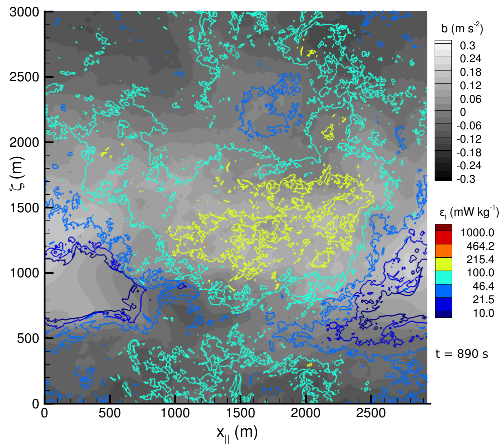

(e) $t = 15\,\text{min}$ (maximum dissipation)

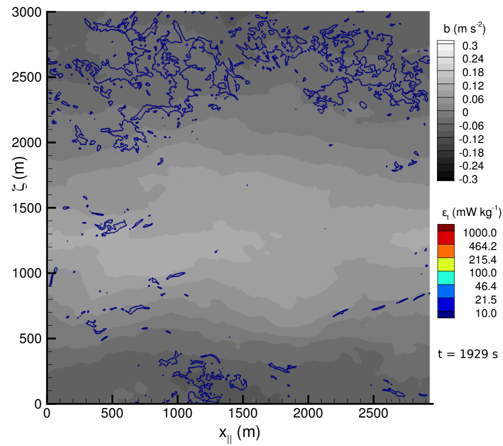

(f) $t = 32\,\text{min}$

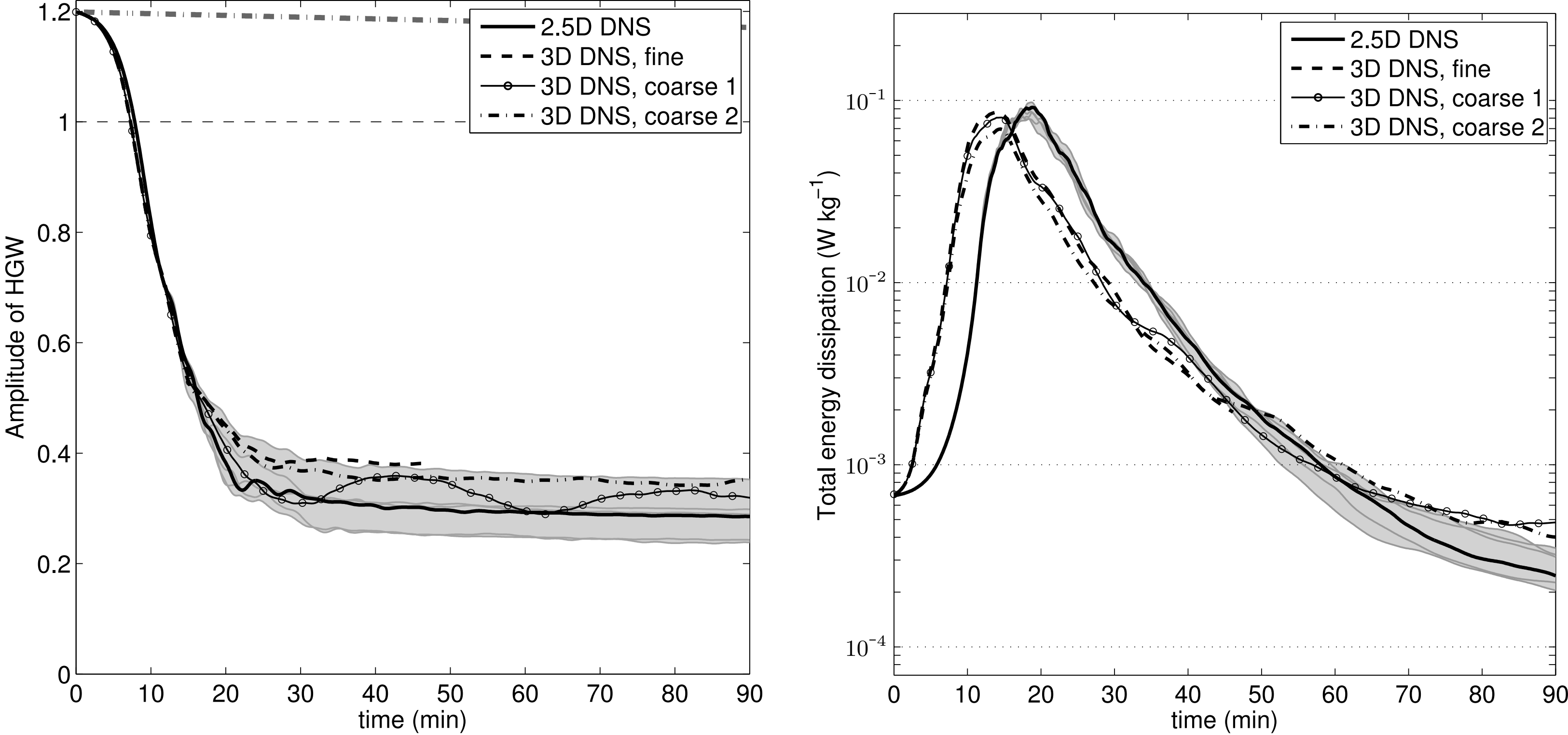

Amplitude of HGW
time (min)
2.5D DNS
3D DNS, fine
3D DNS, coarse 1
3D DNS, coarse 2
Total energy dissipation (W kg^{-1})
time (min)
2.5D DNS
3D DNS, fine
3D DNS, coarse 1
3D DNS, coarse 2

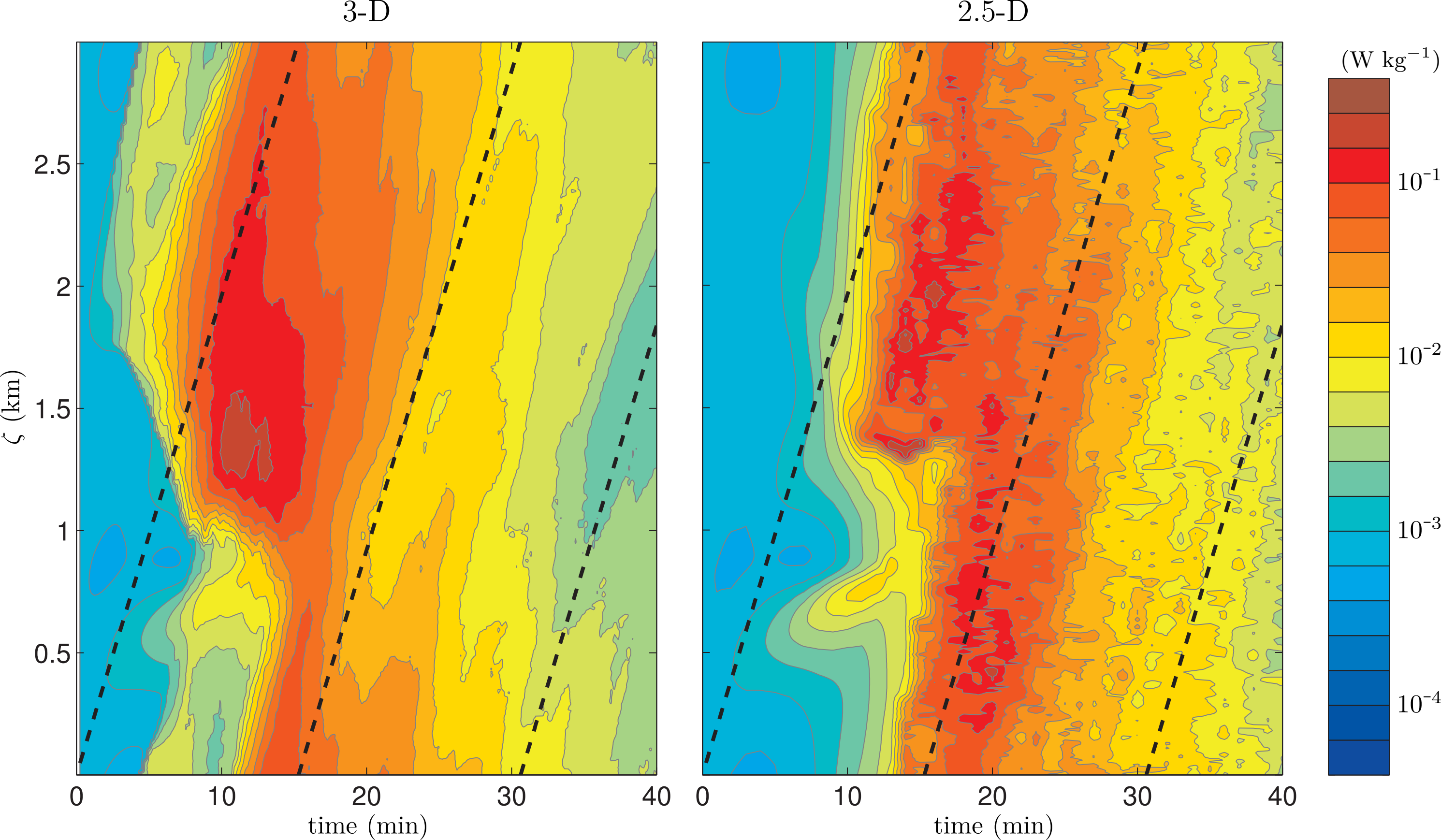
3-D
2.5-D
ζ (km)
0.5
1
1.5
2
2.5
0
10
20
30
40
time (min)
(W kg^{-1})
10^{-1}
10^{-2}
10^{-3}
10^{-4}

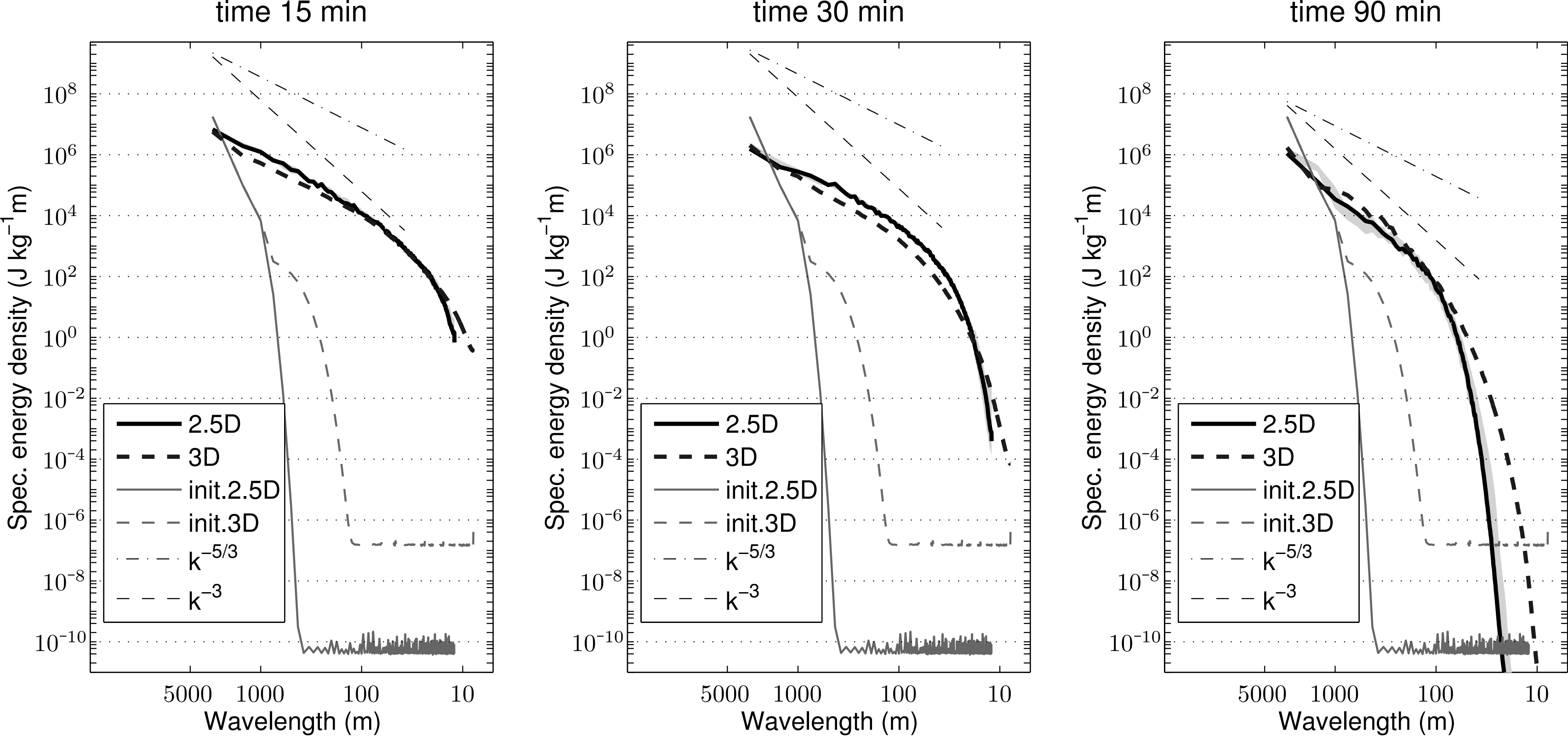

time 15 min
time 30 min
time 90 min
Spec. energy density (J kg^{-1} m)
Wavelength (m)
5000
1000
100
10
10^{8}
10^{6}
10^{4}
10^{2}
10^{0}
10^{-2}
10^{-4}
10^{-6}
10^{-8}
10^{-10}
2.5D
3D
init.2.5D
init.3D
$k^{-5/3}$
k^{-3}